

¹
² Susceptible host dynamics explain pathogen resilience to
³ perturbations

⁴
⁵ Sang Woo Park^{1,*} Bjarke Frost Nielsen² Emily Howerton² Bryan T. Grenfell^{2,3,4}
⁶ Sarah Cobey¹

⁷ **1** Department of Ecology and Evolution, University of Chicago, Chicago, IL, USA

⁸ **2** Department of Ecology and Evolutionary Biology, Princeton University,
Princeton, NJ, USA

¹⁰ **3** High Meadows Environmental Institute, Princeton University, Princeton, NJ,
USA

¹² **4** Princeton School of Public and International Affairs, Princeton, NJ, USA

¹³ *Corresponding author: swp2@uchicago.edu

¹⁴ **Abstract**

¹⁵ A major priority for epidemiological research in the time of anthropogenic change
¹⁶ is understanding how infectious disease dynamics respond to perturbations. Inter-
¹⁷ ventions to slow the spread of SARS-CoV-2 significantly disrupted the transmission
¹⁸ of other human pathogens. As interventions lifted, whether and when respiratory
¹⁹ pathogens would eventually return to their pre-pandemic dynamics remains to be
²⁰ answered. Here, we present a framework for estimating pathogen resilience based
²¹ on how fast epidemic patterns approach their pre-pandemic, endemic dynamics and
²² analyze time series data from Hong Kong, Canada, Korea, and the US. By quanti-
²³ fying the resilience of common respiratory pathogens, we are able to predict when
²⁴ each pathogen will eventually return to pre-pandemic dynamics. Our predictions
²⁵ closely match the observed deviations (or lack thereof) from its pre-COVID dynam-
²⁶ ics. Discrepancies between predicted and observed dynamics indicate the long-term
²⁷ impacts of pandemic perturbations, suggesting that some pathogens may be con-
²⁸ verging to a different endemic cycle. Finally, we show that the replenishment rate
²⁹ of the susceptible pool is a key determinant of pathogen resilience, which in turn
³⁰ determines the sensitivity of a system to stochastic perturbations. Overall, our anal-
³¹ ysis highlights the persistent nature of common respiratory pathogens compared to
³² vaccine-preventable infections, such as measles.

Introduction

34 Non-pharmaceutical interventions to slow the spread of SARS-CoV-2 disrupted the
 35 transmission of other human respiratory pathogens, adding uncertainties to their future
 36 epidemic dynamics and their public health burden [1]. As interventions lifted,
 37 large heterogeneities in outbreak dynamics were observed across different pathogens
 38 in different countries, with some pathogens exhibiting earlier and faster resurgences
 39 than others [2, 3, 4]. Heterogeneities in the overall reduction in transmission and the
 40 timing of re-emergence likely reflect differences in intervention patterns, pathogen
 41 characteristics, immigration/importation from other countries, and pre-pandemic
 42 pathogen dynamics [5]. Therefore, comparing the differential impact of the pandemic
 43 perturbations across pathogens can provide unique opportunities to learn
 44 about underlying pathogen characteristics, such as their transmissibility or duration
 45 of immunity, from heterogeneities in re-emergence patterns [6].

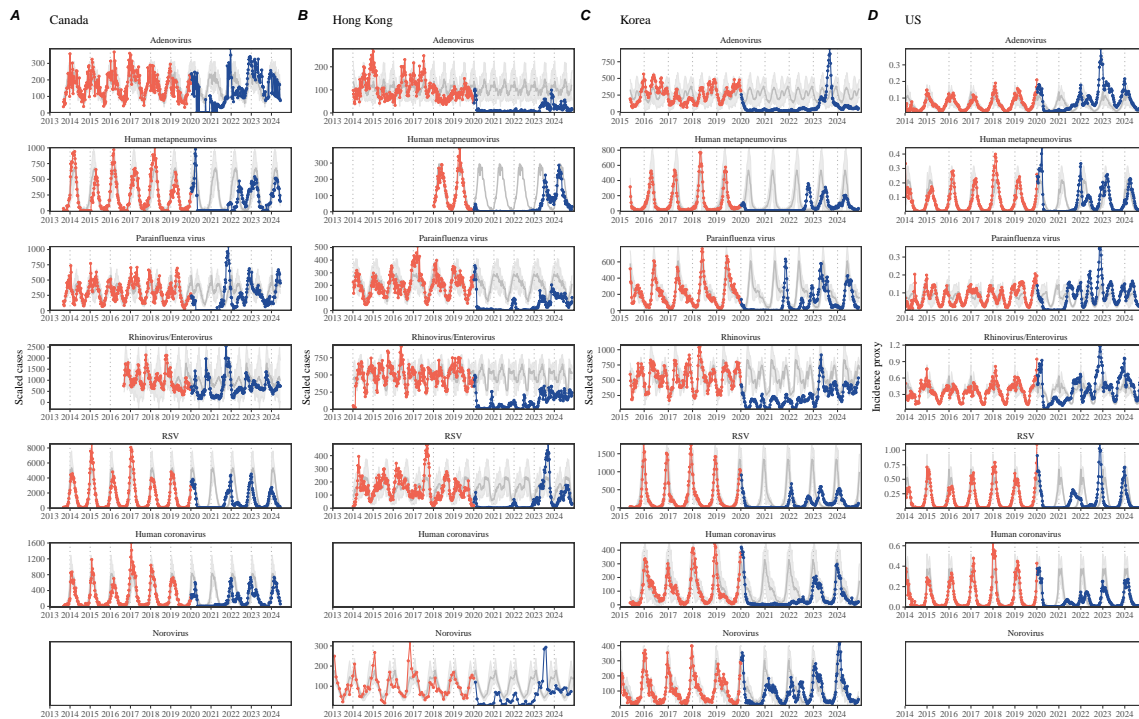


Figure 1: **Observed heterogeneity in responses to pandemic perturbations across respiratory pathogens and norovirus in (A) Canada, (B) Hong Kong, (C) Korea, and (D) US.** Red points and lines represent data before 2020. Blue points and lines represent data since 2020. Gray lines and shaded regions represent the mean seasonal patterns and corresponding 95% confidence intervals around the mean. Mean seasonal patterns were calculated by aggregating cases before 2020 into 52 weekly bins and taking the average in each week. Cases were scaled to account for changes in testing patterns (Materials and Methods).

46 Even though more than five years have passed since the emergence of SARS-CoV-
47 2, we still observe persistent changes in pathogen dynamics following the pandemic
48 perturbations. For example, compared to pre-pandemic, seasonal patterns, human
49 metapneumovirus in Korea seems to circulate at lower levels, whereas RSV in Korea
50 seems to exhibit different seasonality (Figure 1). These observations suggest a fun-
51 damental change in pathogen dynamics following the pandemic perturbations, which
52 might be driven by a long-term shift in either human behavior or population-level
53 immunity [7, 8]. For example, the emergence of SARS-CoV-2 could have caused
54 a long-term shift in population-level immunity through its interactions with other
55 pathogens [9], especially with seasonal coronaviruses [7, 10, 11]. The possibility of a
56 long-lasting impact of the pandemic perturbations poses an important question for
57 future infectious disease dynamics: can we predict whether and when other pathogens
58 will eventually return to their pre-pandemic dynamics?

59 So far, most analyses of respiratory pathogens after pandemic perturbations have
60 focused on characterizing the timing of rebound [1, 12, 5]. Instead, we seek to char-
61 acterize how fast (and whether) a pathogen returns to its pre-pandemic dynamics.
62 These two concepts have a subtle but important difference. For example, it took
63 more than 3 years for human metapneumovirus to rebound in Hong Kong, but the
64 observed epidemic patterns in 2024 appear similar to pre-pandemic seasonal means,
65 suggesting a possible return to pre-pandemic dynamics, though confirmation may
66 require multiple seasons (Figure 1). Measuring this rate of return is useful because it
67 allows us to quantify the ecological resilience of a host-pathogen system, which can
68 inform responses to future interventions [13, 14, 15, 16].

69 In this study, we lay out theoretical and statistical approaches to characterizing
70 the resilience of a host-pathogen system based on how fast the system recovers from
71 perturbation. We begin by laying out a few representative scenarios that capture
72 the potential impact of pandemic perturbations on endemic pathogen dynamics and
73 illustrate how resilience can be measured by comparing the pre- and post-pandemic
74 dynamics of susceptible and infected hosts. In practice, information on suscepti-
75 ble hosts is often unavailable, making this theoretical approach infeasible. Instead,
76 we utilize a mathematical technique to reconstruct empirical attractors from the
77 data [17], which allows us to measure the rate at which the host-pathogen system
78 approaches this empirical attractor after a perturbation; we define this rate to be
79 the empirical resilience of the host-pathogen system. We use this method to ana-
80 lyze pathogen surveillance data for respiratory and non-respiratory pathogens from
81 Canada, Hong Kong, Korea, and the US. Finally, we show that susceptible host dy-
82 namics explain variation in pathogen resilience and further demonstrate that more
83 resilient pathogens will be less sensitive to perturbations caused by demographic
84 stochasticity, thereby providing a direct link between pathogen resilience and persis-
85 tence.

86 **Conceptual introduction to pathogen resilience**

87 In classical ecological literature, the resilience of an ecological system is measured by
88 the rate at which the system returns to its reference state following a perturbation
89 [13, 14, 15, 16]. This rate corresponds to the largest real part of the eigenvalues
90 of the linearized system near equilibrium—here, we refer to this value as the *intrinsic*
91 resilience of the system, which represents the expected rate of return from
92 perturbed states. In practice, we rarely know the true model describing population-
93 level dynamics of common respiratory pathogens, limiting our ability to infer the
94 intrinsic resilience of a system. Instead, we can measure the *empirical* resilience
95 of a host-pathogen system by looking at how fast the system returns to the pre-
96 perturbation, endemic dynamics after the perturbation has ended. The COVID-19
97 pandemic provides a particularly useful example of a major perturbation, providing
98 unique opportunities to measure the resilience of a host-pathogen system.

99 **Resilience of a single-strain system.** As an example, we begin with a sim-
100 ple Susceptible-Infected-Recovered-Susceptible (SIRS) model with seasonally forced
101 transmission and demography (i.e., birth and death). The SIRS model is the simplest
102 model that allows for the waning of immunity and is commonly used for modeling
103 the dynamics of respiratory pathogens [18]. First, consider a pandemic perturbation
104 that reduces transmission by 50% for 6 months starting in 2020, which causes epi-
105 demic patterns to deviate from their original stable annual cycle for a short period of
106 time and eventually come back (Figure 2A). To measure the resilience of this system
107 empirically, we first need to be able to measure the distance from its pre-pandemic
108 attractor, which is defined as a set of points in state space or phase plane that the
109 system is pulled towards [19]. There are many ways we can measure the distance from
110 the attractor, but for illustrative purposes, we choose one of the most parsimonious
111 approaches: that is, we look at how the susceptible (S) and infected (I) populations
112 change over time and measure the Euclidean distance on the SI phase plane, using
113 the counterfactual unperturbed phase plane as a reference (Figure 2B; Materials and
114 Methods). In this simple case, the locally estimated scatterplot smoothing (LOESS)
115 fit indicates that the distance from the attractor decreases exponentially (linearly on
116 a log scale) on average (Figure 2C). Furthermore, the overall rate of return approxi-
117 mates the intrinsic resilience of the seasonally unforced system (Figure 2C).

118 Alternatively, pandemic perturbations can have a lasting impact on the forces
119 driving pathogen dynamics through a long-term reduction in transmission or per-
120 manent change in immunity. As an example, we consider a scenario in which a 10%
121 reduction in transmission persists even after the major pandemic perturbations are
122 lifted (Figure 2D–F). In such cases, we cannot know whether the pathogen will re-
123 turn to its original cycle or a different cycle until many years have passed, and we
124 cannot measure the distance to the new unknown attractor that the system might
125 eventually approach. Nonetheless, we can still measure the distance from the pre-
126 pandemic attractor and ask how the distance changes over time (Figure 2E). The
127 LOESS fit suggests that the distance from the pre-pandemic attractor will initially

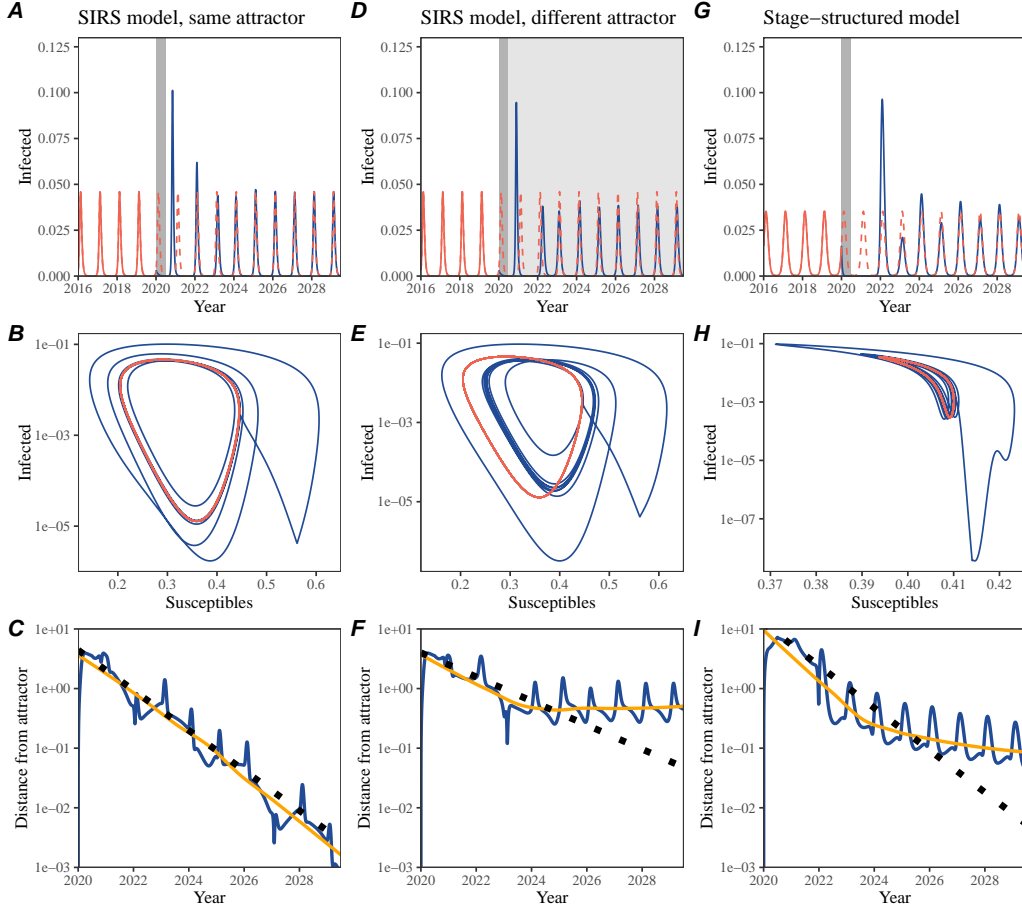


Figure 2: A simple method to measure pathogen resilience following pandemic perturbations across different scenarios. (A, D, G) Simulated epidemic trajectories across various models. Red and blue solid lines represent epidemic dynamics before and after pandemic perturbations are introduced, respectively. Red dashed lines represent counterfactual epidemic dynamics in the absence of perturbations. Gray regions indicate the duration of perturbations with the dark gray region representing a 50% transmission reduction and the light gray region representing a 10% transmission reduction. (B, E, H) Phase plane representation of the time series in panels A, D, and G alongside the corresponding susceptible host dynamics. Red and blue solid lines represent epidemic trajectories on an SI phase plane before and after perturbations are introduced, respectively. (C, F, I) Changes in distance from the attractor over time on a log scale. Blue lines represent the distance from the attractor. Orange lines represent the locally estimated scatterplot smoothing (LOESS) fits to the logged distance from the attractor. Dotted lines show the intrinsic resilience of the seasonally unforced system.

128 decrease exponentially on average (equivalently, linearly on a log scale) and even-
129 tually plateau (Figure 2F). Here, a permanent 10% reduction in transmission rate
130 slows the system, which causes the distance from the pre-pandemic attractor initially
131 to decrease at a slower rate (Figure 2F) than it would have otherwise (Figure 2C)
132 before plateauing at a fixed distance between the two attractors. This example shows
133 that resilience is not necessarily an intrinsic property of a specific pathogen. Instead,
134 pathogen resilience is a property of a specific attractor that a host-pathogen system
135 approaches, which depends on both pathogen and host characteristics.

136 Finally, transient phenomena can further complicate the picture (Figure 2G–I).
137 For example, a stage-structured model, which accounts for reduction in secondary
138 susceptibility, initially exhibits a stable annual cycle, but perturbations from a 10%
139 reduction in transmission for 6 months cause the epidemic to shift to biennial cycles
140 (Figure 2G). The system eventually approaches the original pre-pandemic attractor
141 (Figure 2H), suggesting that this biennial cycle is a transient phenomenon. The
142 LOESS fit indicates that the distance from the attractor initially decreases expo-
143 nentially at a rate that is consistent with the intrinsic resilience of the seasonally
144 unforced stage-structured system, but the approach to the attractor slows down
145 with the damped oscillations (Figure 2I). This behavior is also referred to as a ghost
146 attractor, which causes long transient dynamics and slow transitions [20]. Strong
147 seasonal forcing in transmission can also lead to transient phenomena for a simple
148 SIRS model, causing a slow return to pre-perturbation dynamics (Supplementary
149 Figure S1).

150 **Resilience of a two-strain system.** This empirical approach allows us to
151 measure the resilience of a two-strain host-pathogen system as well even when we
152 have incomplete observation of the infection dynamics. Simulations from a simple
153 two-strain competition system illustrate that separate analyses of individual strain
154 dynamics (e.g., RSV A vs B) and a joint analysis of total infections (e.g., total
155 RSV infections) yield identical resilience estimates (Supplementary Figure S2, 3).
156 This is expected because eigenvalues determine the dynamics of the entire system
157 around the equilibrium, meaning that both strains should exhibit identical rates of
158 return following a perturbation. However, these conclusions likely depend on the
159 strength of strain interaction as well as the underlying details of the model. For
160 example, ecological interference between two unrelated pathogens [21] will likely
161 generate weaker coupling than cross immunity between related pathogens; in the
162 former case, we do not necessarily expect two unrelated pathogens to have same
163 resilience despite their ecological interference. For simplicity, we focus on a simple,
164 two-strain model with cross immunity in this paper. Analogous to a single-strain
165 system, strong seasonal forcing in transmission can cause the two-strain system to
166 slow down through transient phenomena (Supplementary Figure S4).

167 These observations yield three insights. First, we can directly estimate the empi-
168 rical resilience of a host-pathogen system by measuring the rate at which the system
169 approaches an attractor, provided that we have a way to quantify the distance from
170 the attractor—as we discuss later, the attractor of a system can be reconstructed

from data from mathematical theory without making assumptions about the underlying model. The empirical approach to estimating pathogen resilience is particularly convenient because it does not require us to know the true underlying model; estimating the intrinsic resilience from fitting misspecified models can lead to biased estimates (Supplementary Figure S5). Second, resilience estimates allow us to make phenomenological predictions about the dynamics of a host-pathogen system following a perturbation. Assuming that an attractor has not changed and the distance from the attractor will decrease exponentially over time, we can estimate when the system should reach an attractor. Finally, a change in the (exponential) rate of approach provide information about whether the system has reached an alternative attractor, or a ghost attractor, that is different from the original, pre-pandemic attractor. These alternative attractors may reflect permanent changes in transmission patterns as well as changes in immune landscapes. There will be periods of time when it is difficult to tell whether pathogen dynamics are still diverging from the original attractor due to a long-term perturbation, or have entered the basin of attraction of a new attractor. Now that several years have passed since major interventions have been lifted, many respiratory pathogens may have had sufficient time to begin returning to their post-intervention attractors—empirical comparisons between current cases and pre-pandemic cases are consistent with this hypothesis (Figure 1). With recent data, we can start to evaluate whether we see early signs of convergence to the former attractor or a new one.

Inferring pathogen resilience from real data

Based on these observations, we now lay out our approach to estimating pathogen resilience from real data (Figure 3). We first tested this approach against simulations and applied it to real data. Specifically, we analyzed case time series of respiratory pathogens from four countries: Canada, Hong Kong, Korea, and the US.

So far, we have focused on simple examples that assume a constant transmission reduction during the pandemic. However, in practice, the impact of pandemic perturbations on pathogen transmission was likely more complex (Figure 3A), reflecting introduction and relaxation of various intervention strategies. In some cases, strong perturbations likely caused local fadeouts, requiring immigration/importation from another location for epidemic rebound. Such complexities could lead to longer delays between the introduction of pandemic perturbations and pathogen rebound as well as temporal variation in outbreak sizes (Figure 3B); in this example, continued transmission reduction from interventions limits the size of the first outbreak in 2021 following the rebound, allowing for a larger outbreak in 2022 when interventions are further relaxed.

Previously, we relied on the dynamics of susceptible and infected hosts to compute the distance from the attractor (Figure 2), but information on susceptible hosts is rarely available in practice. In addition, uncertainties in case counts due to ob-

211 servation error, strain evolution, and multiannual cycles in the observed epidemic
212 dynamics (e.g., adenovirus circulation patterns in Hong Kong and Korea) add chal-
213 lenges to defining pre-pandemic attractors, which limits our ability to measure the
214 distance from the attractor. To address these challenges, we can reconstruct an em-
215 pirical attractor by utilizing Takens' theorem [17], which states that an attractor of a
216 nonlinear multidimensional system can be mapped onto a delayed embedding (Mate-
217 rials and Methods). For example, we can use delayed logged values of pre-pandemic
218 cases $C(t)$ (Figure 3C) to reconstruct the attractor:

$$\langle \log(C(t) + 1), \log(C(t - \tau) + 1), \dots, \log(C(t - (M - 1)\tau) + 1) \rangle, \quad (1)$$

219 where the delay τ and embedding dimension M are determined based on autocor-
220 relations and false nearest neighbors, respectively [22, 23]. This allows us to define
221 the pre-pandemic attractor as a points on an M dimensional space. We can then
222 apply the same delay and embedding dimensions to the entire time series to deter-
223 mine the position in multi-dimensional state space (Figure 3D), which allows us to
224 measure the nearest neighbor distance between the current state of the system and
225 the empirical pre-pandemic attractor (Figure 3E). Specifically, the nearest neighbor
226 distance is calculated by computing the distance between the current position on
227 the M dimensional space and all points in the empirical attractor set and taking the
228 minimum value. In theory, we can now quantify how fast this distance decreases by
229 fitting a linear regression on a log scale, where the slope of the linear regression em-
230 pirically measures pathogen resilience with a steeper slope corresponding to a higher
231 resilience estimate (Figure 3E). However, resulting estimates of pathogen resilience
232 can be sensitive to choices about embedding delays and dimensions. For example,
233 using longer delays and higher dimensions tends to smooth out temporal variations
234 in the distance from the attractor (Supplementary Figure S6).

235 Complex changes in the distance from the attractor suggest that estimating
236 pathogen resilience from linear regression will be particularly sensitive to our choice
237 of fitting windows for the regression (Figure 3E). Therefore, before we tried estimat-
238 ing resilience from real data, we explored an automated window selection criterion
239 for linear regression and tested it against randomized, stochastic simulations across
240 a range of realistic pandemic perturbation shapes. In doing so, we also explored
241 optimal choices for embedding dimensions and evaluated our choices of fitting win-
242 dows parameters and embedding dimensions by quantifying correlation coefficients
243 between the estimated resilience and the intrinsic resilience of a seasonally unforced
244 system (Materials and Methods). Overall, we found large variation in estimation
245 performances with correlation coefficient ranging from 0.21 to 0.61 (Supplementary
246 Figure S7). In almost all cases, the automated window selection approach outper-
247 formed a naive approach, which performs regression between the peak distance and
248 current distance (Supplementary Figure S7).

249 Based on the best performing window selection criteria and embedding dimen-
250 sion, we applied this approach to pathogen surveillance data presented in Figure
251 1 (Materials and Methods). For each time series, we applied Takens' theorem in-

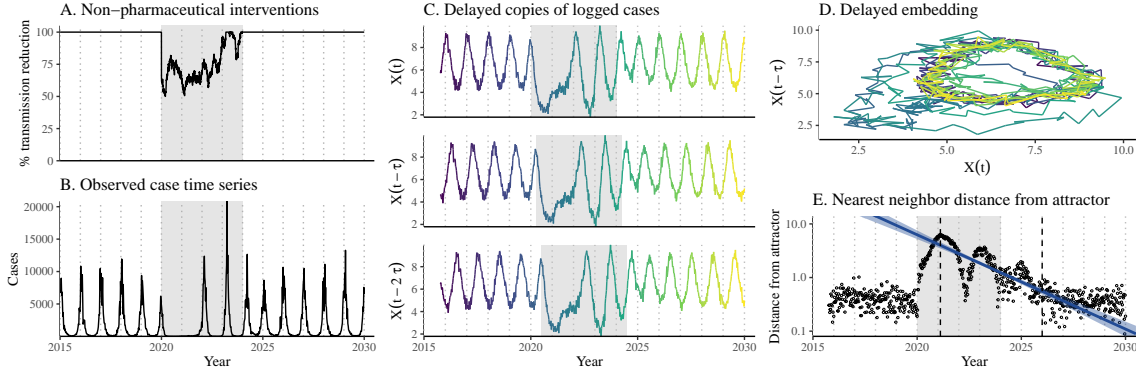


Figure 3: **A schematic diagram explaining the inference of pathogen resilience from synthetic data.** (A) A realistic example of simulated pandemic perturbations, represented by a relative reduction in transmission. (B) The impact of the synthetic pandemic perturbation on epidemic dynamics simulated using a SIRS model with demographic stochasticity. (C) Generating delayed copies of the logged time series allows us to obtain an embedding. (D) Two dimensional representation of an embedding. (E) Delayed embedding allows us to calculate the nearest neighbor distance from the empirical attractor, which is determined based on the pre-pandemic time series. Blue lines and dashed regions represent the linear regression fit and the associated 95% confidence interval. This distance time series can be used to infer pathogen resilience after choosing an appropriate window for linear regression. For illustration purposes, an arbitrary fitting window was chosen.

dependently to reconstruct the empirical attractor and obtained the corresponding time series of distances from attractors (Supplementary Figure S8). Then, we used the automated window selection criterion to fit a linear regression and estimated the empirical resilience for each pathogen in each country (Supplementary Figure S8); the window selection criterion gave poor regression window for three cases (norovirus in Hong Kong and Korea and rhinovirus/enterovirus in the US), leading to unrealistically low resilience estimates, and so we used ad-hoc regression windows instead (Supplementary Figure S9; Materials and Methods).

For all pathogens we considered, resilience estimates fell between 0.4/year and 1.8/year (Figure 4A). We estimated the mean resilience of common respiratory pathogens to be 0.99/year (95% CI: 0.81/year–1.18/year). For reference, this is ≈ 7.5 times higher than the intrinsic resilience of pre-vaccination measles in England and Wales ($\approx 0.13/\text{year}$). Finally, resilience estimates for norovirus, a gastrointestinal pathogen, were comparable to those of common respiratory pathogens: 1.44/year (95% CI: 1.01/year–1.87/year) for Hong Kong and 1.07/year (95% CI: 0.86/year–1.29/year) for Korea. Based on a simple ANOVA test, we did not find significant differences in resilience estimates across countries ($p = 0.25$) or pathogens ($p = 0.67$).

Using resilience estimates, we predicted when each pathogen would hypothetically return to their pre-pandemic dynamics, assuming no long-term change in the attrac-

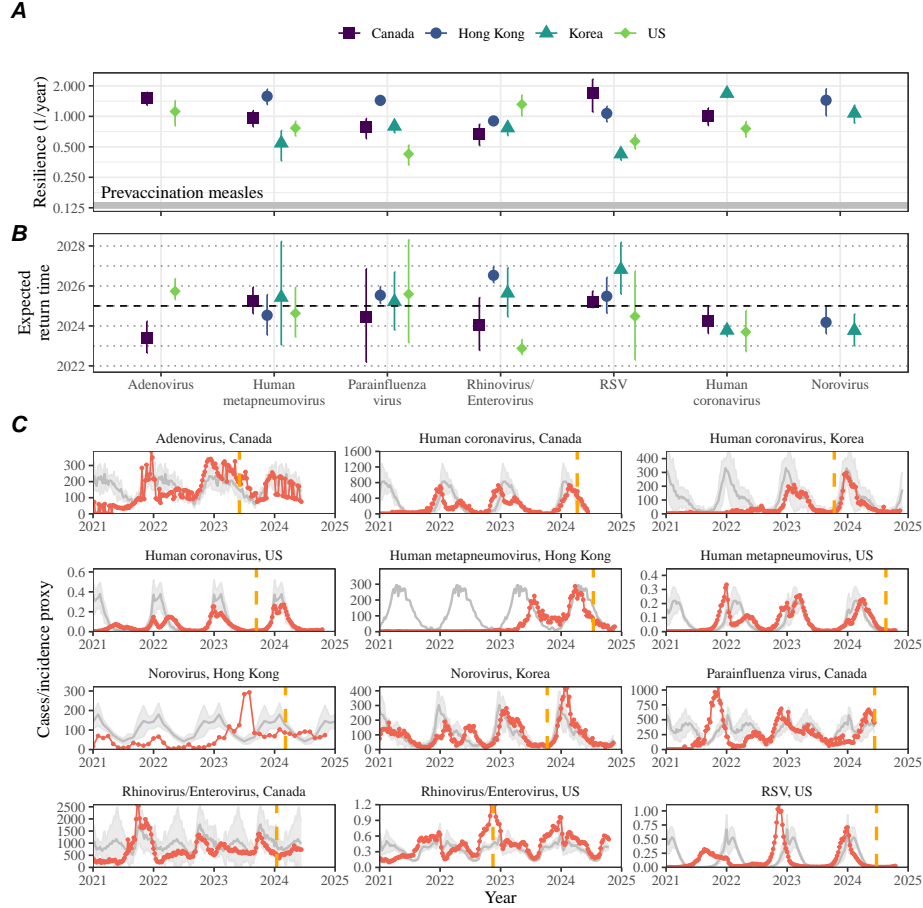


Figure 4: **Summary of resilience estimates and predictions for return time.** (A) Estimated pathogen resilience. The gray horizontal line represents the intrinsic resilience of pre-vaccination measles dynamics. (B) Predicted timing of when each pathogen will return to their pre-pandemic cycles. The dashed line in panel B indicates the end of 2024. Error bars represent 95% confidence intervals. (C) Observed dynamics for pathogen that are predicted to have returned before the end of 2024. Red points and lines represent data before 2020. Gray lines and shaded regions represent the mean seasonal patterns and corresponding 95% confidence intervals around the mean, previously shown in Figure 1. Orange vertical lines represent the predicted timing of return.

271 tor. Specifically, we extended our linear regression fits to distance-from-attractor
 272 time series and ask when the predicted regression line will cross a threshold value;
 273 since we relied on nearest neighbor distances, pre-pandemic distances are always
 274 greater than zero (Figure 3E), meaning that we can use the mean of pre-pandemic
 275 distances as our threshold.

276 We predicted that a return to pre-pandemic cycles has occurred or would be

imminent for most pathogens (Figure 4B). In particular, we predicted that 12 out of 23 pathogen-country pairs should have already returned before the end of 2024. For almost all pathogens that were predicted to have returned already, the observed epidemic dynamics showed clear convergence towards their pre-pandemic seasonal averages, confirming our predictions (Figure 4C). However, there were a few exceptions, including norovirus in Hong Kong and rhinovirus/enterovirus in the US, where the observed epidemic dynamics in 2024 exhibit clear deviation from their pre-pandemic seasonal averages (Figure 4C; Figure S9). These observations suggest a possibility that some common respiratory pathogens may have converged to different attractors or are still exhibiting non-equilibrium dynamics. In contrast, pathogens that were predicted to have not returned yet also showed clear differences from their pre-pandemic seasonal averages; as many of these pathogens are predicted to return in 2025–2026, we may be able to test these predictions in near future (Supplementary Figure S10). Our reconstructions of distance time series and estimates of pathogen resilience and expected return time were generally robust to choices of embedding dimensions (Supplementary Figure S11–12).

Susceptible host dynamics explain variation in pathogen resilience

So far, we have focused on quantifying pathogen resilience from the observed patterns of pathogen re-emergence following pandemic perturbations. But what factors determine how resilient a host-pathogen system is? To address this question, we used the SIRS model to explore how changes in susceptible host dynamics affect pathogen resilience. To do so, we varied the basic reproduction number \mathcal{R}_0 , which represents the average number of secondary infections caused by a newly infected individual in a fully susceptible population, and the duration of immunity and computed intrinsic resilience for each parameter.

We found that an increase in \mathcal{R}_0 and a decrease in the duration of immunity correspond to an increase in pathogen resilience (Figure 5A). Similarly, an increase in \mathcal{R}_0 and a decrease in the duration of immunity corresponds to a faster per-capita rate of susceptible replenishment, which is defined as the ratio between absolute rate at which new susceptibles enter the population and the equilibrium number of susceptible individuals in the population, S^* (Figure 5B). We note that a higher \mathcal{R}_0 drives a faster per-capita susceptible replenishment rate by decreasing the susceptible proportion at equilibrium, S^* . For a simple SIR model that assumes a life-long immunity, we can show analytically that pathogen resilience is proportional to the per-capita rate of susceptible replenishment (Materials and Methods). Overall, these observations suggest that a faster per-capita susceptible replenishment rate causes the system to be more resilient.

By taking the average values of empirical resilience values for each pathogen, we were able to map each pathogen onto a set of parameters of the SIRS model that are

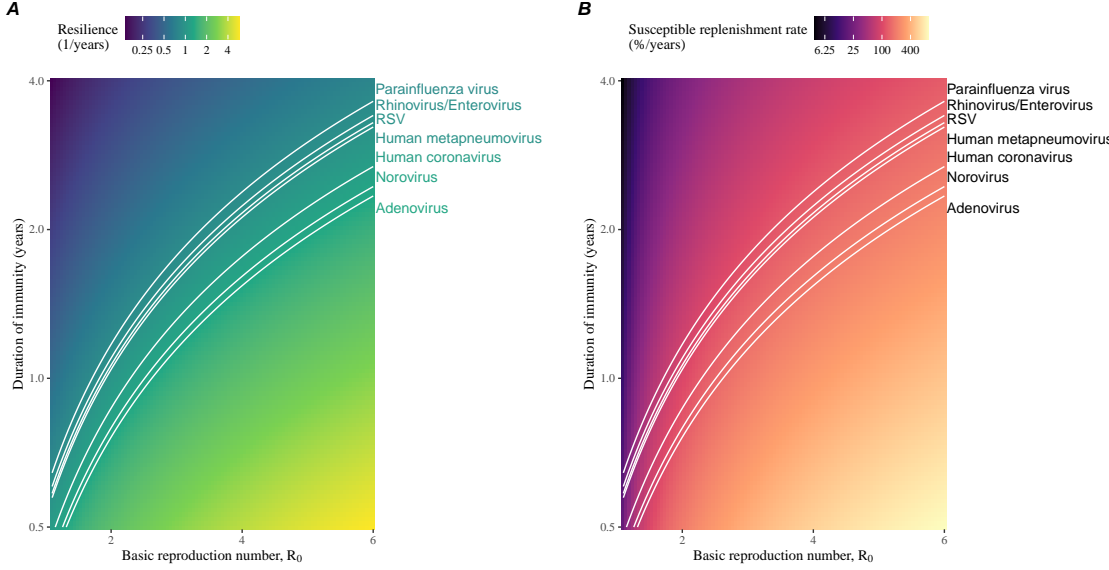


Figure 5: Linking pathogen resilience to epidemiological parameters and susceptible host dynamics. (A) Intrinsic resilience as a function of the basic reproduction number \mathcal{R}_0 and the duration of immunity. (B) Per-capita susceptible replenishment rate as a function of the basic reproduction number \mathcal{R}_0 and the duration of immunity. The standard SIRS model without seasonal forcing is used to compute intrinsic resilience and the per-capita susceptible replenishment rate. Lines correspond to a set of parameters that are consistent with mean resilience estimates for each pathogen, averaged across different countries.

317 consistent with corresponding resilience estimates (Figure 5A). Across all pathogens
 318 we considered, we estimated that the average duration of immunity is likely to be
 319 short (< 4 years) across a plausible range of \mathcal{R}_0 (< 6). We were also able to obtain
 320 a plausible range of susceptible replenishment rates for each pathogen (Figure 5B),
 321 but there was a large uncertainty in the estimates for susceptible replenishment rates
 322 due to a lack of one-to-one correspondence between susceptible replenishment rates
 323 and pathogen resilience.

324 **Pathogen resilience determines sensitivity to stochastic perturbations**

326 Even in the absence of major pandemic perturbations, host-pathogen systems are
 327 expected to experience continued perturbations of varying degrees from changes in
 328 epidemiological conditions, such as human behavior, climate, and viral evolution.
 329 These perturbations can also arise from demographic stochasticity, which is inherent
 330 to any ecological systems. Here, we used a seasonally unforced SIRS model

331 with birth/death to explore how resilience of a host-pathogen system determines
 332 the sensitivity to perturbations caused by demographic stochasticity (Materials and
 333 Methods).

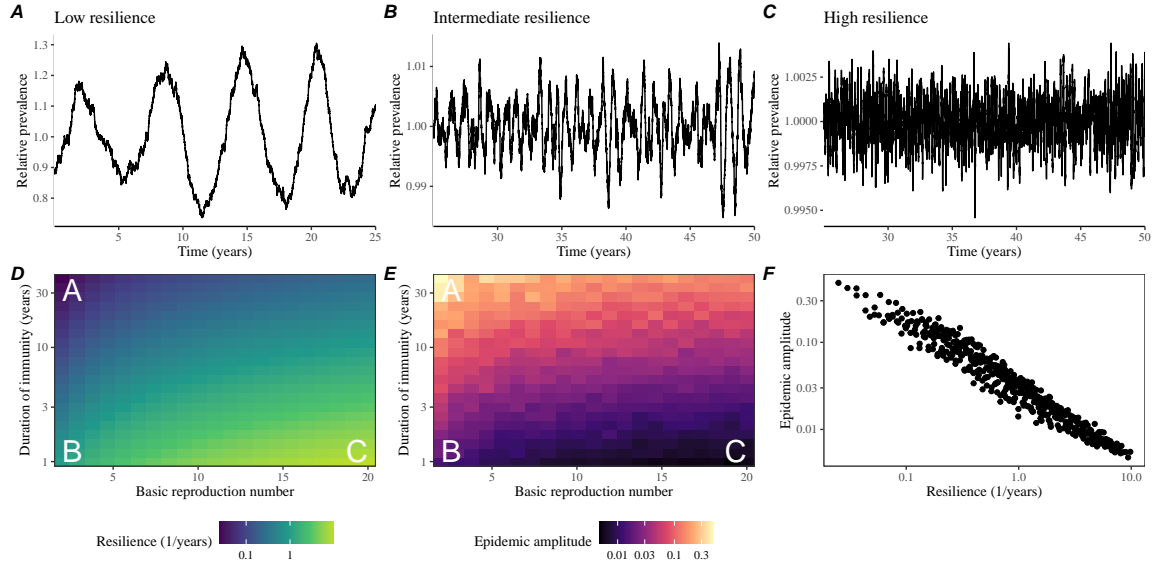


Figure 6: **Linking resilience of a host-pathogen system to its sensitivity to stochastic perturbations.** (A–C) Epidemic trajectories of a stochastic SIRS model across three different resilience values: low, intermediate, and high. The relative prevalence was calculated by dividing infection prevalence by its mean value. (D) Intrinsic resilience of a system as a function of the basic reproduction number \mathcal{R}_0 and the duration of immunity. (E) Epidemic amplitude as a function of the basic reproduction number \mathcal{R}_0 and the duration of immunity. The epidemic amplitude corresponds to $(\max I - \min I)/(2\bar{I})$, where \bar{I} represents the mean prevalence. Labels A–C in panels D and E correspond to scenarios shown in panels A–C. (F) The relationship between pathogen resilience and epidemic amplitude.

334 We found that resilience of a host-pathogen system determines the amount of de-
 335 viation from the deterministic trajectory caused by demographic stochasticity, with
 336 less resilient systems experiencing larger deviations (Figure 6). Notably, less resilent
 337 systems also exhibited slower epidemic cycles (Figure 6A–C). The periodicity of this
 338 epidemic cycle matched those predicted by the intrinsic periodicity of the system
 339 (Supplementary Figure S13) where the intrinsic resilience of the system is inversely
 340 proportional to its intrinsic periodicity (Supplementary Figure S14). However, we
 341 note that the interplay between seasonal transmission and intrinsic periodicity can
 342 also lead to complex cycles, as illustrated by a recent analysis of *Mycoplasma pneumoniae*
 343 dynamics [24].

344 We also note that the intrinsic resilience is not the sole determinant for how sen-
 345 sitive the system is to stochastic perturbations. For example, the population size

346 and average duration of infection also affect the amount of deviation from the deter-
347 ministic trajectory caused by demographic stochasticity, even though these quantities
348 have little to no impact on the intrinsic resilience (Supplementary Figure S15). These
349 conclusions were robust for the seasonally forced SIRS model (Supplementary Figure
350 S16).

351 Discussion

352 COVID-19 pandemic interventions caused major disruptions to circulation patterns
353 of both respiratory and non-respiratory pathogens, adding challenges to predicting
354 their future dynamics [1, 2, 3, 4]. However, these perturbations offer large-scale natu-
355 ral experiments for understanding how different pathogens respond to perturbations.
356 In this study, we showed that pathogen re-emergence patterns following pandemic
357 perturbations can be characterized through the lens of ecological resilience and pre-
358 sented a new method for estimating pathogen resilience from time series data. We
359 showed that variation in pathogen resilience can be explained by the differences in
360 susceptible host dynamics, where faster replenishment of the susceptible pool corre-
361 sponds to a more resilient host-pathogen system. Finally, we showed that pathogen
362 resilience also determines the sensitivity to stochastic perturbations.

363 We analyzed case time series of common respiratory infections and norovirus
364 infections from Canada, Hong Kong, Korea, and the US to estimate their resilience.
365 Overall, we estimated the resilience of these pathogens to range from 0.4/year to
366 1.8/year, which is 3–14 times more resilient than prevaccination measles. Consistent
367 with other epidemiological evidence [25, 26, 27, 28], these resilience estimates indicate
368 that common respiratory pathogens and norovirus likely exhibit faster susceptible
369 replenishment and are therefore more persistent, indicating potential challenges in
370 controlling these pathogens.

371 Based on our resilience estimates, we made phenomenological predictions about
372 when each pathogen will return to their endemic cycles. For the most part, we
373 accurately predicted which pathogens should have already returned before the end
374 of 2024. However, there were two main exceptions (i.e., norovirus in Hong Kong
375 and rhinovirus/enterovirus in the US), suggesting that these pathogens may be con-
376 verging to new endemic cycles or experiencing long-term transient behavior. These
377 changes may reflect changes in surveillance or actual shift in the dynamics, caused
378 by permanent changes in behavior or population-level immunity. While it may seem
379 unlikely that permanent changes in behavior would only affect a few pathogens and
380 not others, we cannot rule out this possibility given differences in the observed mean
381 age of infections and therefore the differences in age groups that primarily drive
382 transmission [29, 30]. Differences in the mode of transmission between respiratory
383 vs gastrointestinal pathogens may also contribute to the differences in responses to
384 pandemic perturbations.

385 For almost half of the pathogens we considered, we predicted that their return

386 to original epidemic patterns is imminent. We will need a few more years of data
387 to test whether these pathogens will eventually return to their original dynamics or
388 eventually converge to a different attractor. We also cannot rule out the possibility
389 that some pathogens may exhibit long-term transient behaviors following pandemic
390 perturbations. Overall, these observations echo earlier studies that highlighted the
391 long-lasting impact of pandemic perturbations [8, 31, 32, 4, 24].

392 We showed that susceptible host dynamics shape pathogen resilience, where faster
393 replenishment of the susceptible population causes the pathogen to be more resilient.
394 For simplicity, we focused on waning immunity and birth as the main drivers of the
395 susceptible host dynamics but other mechanisms can also contribute to the replen-
396 ishment of the susceptible population. In particular, pathogen evolution, especially
397 the emergence of antigenically novel strains, can cause effective waning of immunity
398 in the population; therefore, we hypothesize that the rate of antigenic evolution is
399 likely a key feature of pathogen resilience. Future studies should explore the relation-
400 ship between the rate of evolution and resilience for antigenically evolving pathogens.
401 This result also highlights the importance of detailed measurements of changes in
402 the susceptible population through serological assays for understanding pathogen
403 dynamics [33].

404 Quantifying pathogen resilience also offers novel approaches to validating population-
405 level epidemiological models. So far, most model validation in infectious disease ecol-
406 ogy is based on the ability of a model to reproduce the observed epidemic dynamics
407 and to predict future dynamics [34, 35, 27, 36, 37]. However, many models can
408 perform similarly under these criteria. For example, two major RSV models have
409 been proposed to explain biennial epidemic patterns: (1) a stage- and age-structured
410 model that allows disease severity to vary with number of past infections and age of
411 infection [27] and (2) a pathogen-interaction model that accounts for cross immunity
412 between RSV and human metapneumovirus [35]. Since both models can accurately
413 reproduce the observed epidemic patterns, standard criteria for model validation
414 do not allow us to distinguish between these two models from population-level data
415 alone. Instead, it would be possible to measure the empirical resilience of each model
416 by simulating various perturbations and comparing the simulations to estimates of
417 empirical resilience from data, using pandemic perturbations as a reference.

418 There are several limitations to our work. First, we did not extensively explore
419 other approaches to reconstructing the attractor. Recent studies showed that more
420 sophisticated approaches, such as using non-uniform embedding, can provide more
421 robust reconstruction for noisy data [23]. In the context of causal inference, choices
422 about embedding can have major impact on the resulting inference [38]. Our re-
423 silience estimates are likely overly confident given a lack of uncertainties in attractor
424 reconstruction as well as the simplicity of our statistical framework. Nonetheless,
425 as illustrated in our sensitivity analyses, inferences about pathogen resilience in our
426 SIRS model appear to be robust to decisions about embedding lags and dimensions—
427 this is because tracking the rate at which the system approaches the attractor is likely
428 a much simpler problem than making inferences about causal directionality. Short

429 pre-pandemic time series also limit our ability to accurately reconstruct the attractor
430 and contribute to the crudeness of our resilience estimates; although this is less
431 likely a problem for respiratory pathogens that are strongly annual, our attractor
432 reconstruction may be inaccurate for those exhibiting multi-annual cycles, such as
433 adenovirus in Hong Kong and Korea. Our framework also do not allow us to distin-
434 guish whether a system has settled to a new attractor or is experiencing long-term
435 transient behavior. Uncertainties in pathogen dynamics due to changes in testing
436 patterns further contribute to the crudeness of our resilience estimates.

437 While attractor reconstruction methods allow us to make model-free inferences
438 of pathogen resilience, it does not allow us to tease apart how different mechanisms
439 contribute to the resilience a host-pathogen system. Using simple SIRS model, we
440 illustrated that susceptible host dynamics are key determinants for pathogen re-
441 silience, but we also found that there isn't a one-to-one correspondence between
442 per capita replenishment rate of the susceptible population and pathogen resilience
443 estimates. Future studies should explore using mechanistic models to explain hetero-
444 geneity in resilience estimates across different pathogens. Despite these limitations,
445 our qualitative prediction that common respiratory pathogens are more resilient than
446 prevaccination measles is also likely to be robust, given how rapidly many respiratory
447 pathogens returned to their original cycles following pandemic perturbations.

448 Predicting the impact of anthropogenic changes on infectious disease dynamics
449 is a fundamental aim of infectious disease research in a rapidly changing world. Our
450 study illustrates that how a host-pathogen system responds to both small and large
451 perturbations is largely predictable through the lens of ecological resilience. In par-
452 ticular, quantifying the resilience of a host-pathogen system offers a unique insight
453 into questions about endemic pathogens' responses to pandemic perturbations, in-
454 cluding whether some pathogens will exhibit long-lasting impact from the pandemic
455 perturbation or not. More broadly, a detailed understanding of the determinants of
456 pathogen resilience can provide deeper understanding of pathogen persistence.

457 Materials and Methods

458 Data

459 We gathered time series on respiratory infections from Canada, Hong Kong, Korea,
460 and United States (US). As a reference, we also included time series data on norovirus
461 infections when available. In contrast to respiratory pathogens, we hypothesized
462 gastrointestinal viruses, such as norovirus, to be differently affected by pandemic
463 perturbations.

464 Weekly time series of respiratory infection cases in Canada came from a publicly
465 available website by the Respiratory Virus Detection Surveillance System, which
466 collects data from select laboratories across Canada [39]. Weekly time series of
467 respiratory infection cases in Hong Kong came from a publicly available website by
468 the Centre for Health Protection, Department of Health [40, 41]. Weekly time series

469 of acute respiratory infection cases in Korea came from a publicly available website
470 by the Korea Disease Control and Prevention Agency [42]. Finally, weekly time series
471 of respiratory infection cases in the US were obtained from the National Respiratory
472 and Enteric Virus Surveillance System. Time series on number of tests were also
473 available in Canada, Hong Kong, and the US, but not in Korea.

474 Data processing

475 For all time series, we rounded every year to 52 weeks by taking the average number
476 of cases and tests between the 52nd and 53rd week. We also rescaled all time series to
477 account for changes in testing patterns, which were then used for the actual analysis.

478 For Canada, an increase in testing was observed from 2013 to 2024 (Supplementary
479 Figure S17). To account for this increase, we calculated a 2 year moving average
480 for the number of tests for each pathogen, which we used as a proxy for testing effort.
481 Then, we divided the smoothed testing patterns by the smoothed value at the final
482 week such that the testing effort has a maximum of 1. We then divided weekly cases
483 by the testing effort to obtain a scaled case time series. A similar approach was used
484 earlier for an analysis of RSV time series in the US to account for changes in testing
485 patterns [27].

486 For Hong Kong, we applied the same scaling procedure to the time series as we
487 did for Canada. In this case, we only adjusted for testing efforts up to the end of 2019
488 because there was a major reduction in testing for common respiratory pathogens
489 between 2020 and 2023 (Supplementary Figure S18).

490 For Korea, while we did not have information on testing, the reported number
491 of respiratory infections consistently increased from 2013 to the end of 2019, which
492 we interpreted as changes in testing patterns (Supplementary Figure S19). Since
493 we did not have testing numbers, we used the weekly sum of all acute respiratory
494 viral infection cases as a proxy for testing, which were further smoothed with moving
495 average and scaled to have a maximum of 1. For Korea, we also only adjusted for
496 testing efforts up to the end of 2019.

497 In the US, there has been a large increase in testing for some respiratory pathogens,
498 especially RSV, which could not be corrected by simple scaling (Supplementary Figure
499 S20). Instead, we derived an incidence proxy by multiplying the test positivity
500 with influenza-like illness positivity, which was taken from [https://gis.cdc.gov/
501 grasp/fluvview/fluportaldashboard.html](https://gis.cdc.gov/grasp/fluvview/fluportaldashboard.html). This method of estimating an incidence
502 proxy has been recently applied in the analysis of seasonal coronaviruses [7]
503 and *Mycoplasma pneumoniae* infections [4]. Detailed assumptions and justifications
504 are provided in [43].

505 Data summary

506 To make qualitative comparisons between pre- and post-perturbation dynamics of
507 respiratory pathogen circulation patterns, we calculated the mean seasonal patterns

508 using time series of either rescaled cases or incidence proxy estimates before 2020. We
 509 did so by taking the mean value in each week across all years before 2020. Confidence
 510 intervals around the means were calculated using a simple t test.

511 Estimating pathogen resilience

512 In order to measure pathogen resilience from surveillance data, we first reconstructed
 513 the empirical pre-pandemic attractor of the system using Takens' embedding theorem
 514 [17]. Specifically, for a given pathogen, we took the pre-pandemic (before 2020) case
 515 time series $C(t)$ and reconstructed the attractor using delayed embedding with a
 516 uniform delay of τ and dimension M :

$$X_{\tau,m}(t) = \langle \log(C(t) + 1), \log(C(t - \tau) + 1), \dots, \log(C(t - (M - 1)\tau) + 1) \rangle. \quad (2)$$

517 Here, the delay τ was determined by calculating the autocorrelation of the logged
 518 pre-pandemic time series and asking when the autocorrelation crosses 0 for the first
 519 time [23]; a typical delay for an annual outbreak is around 13 weeks.

520 Then, for a given delay τ , we determined the embedding dimension M using the
 521 false nearest neighbors approach [22, 23]. To do so, we started with an embedding
 522 dimension e and constructed a set of points $A_{\tau,e} = \{X_{\tau,e}(t) | t < 2020\}$. Then, for
 523 each point $X_{\tau,e}(t)$, we determined the nearest neighbor from the set $A_{\tau,e}$, which we
 524 denote $X_{\tau,e}(t_{nn})$ for $t \neq t_{nn}$. Then, if the distance between these two points in the
 525 $e+1$ dimension, $D_{\tau,e+1}(t) = \|X_{\tau,e+1}(t_{nn}) - X_{\tau,e+1}(t)\|_2$, is larger than their distance in
 526 the e dimension, $D_{\tau,e}(t) = \|X_{\tau,e}(t_{nn}) - X_{\tau,e}(t)\|_2$, these two points are deemed to be
 527 false nearest neighbors; specifically, we used a threshold R for the ratio between two
 528 distances $D_{\tau,e+1}(t)/D_{\tau,e}(t)$ to determine false nearest neighbors. The first embed-
 529 ding dimension e that does not have any false nearest neighbors corresponds to the
 530 embedding dimension M for a given pathogen-country pair. For the main analysis,
 531 we used $R = 10$, which was chosen from a sensitivity analysis against simulated data
 532 (Supplementary Text). Once we determined the embedding lag τ and dimension M ,
 533 we apply the embedding to the entire time series and calculate the nearest neigh-
 534 bor distance against the attractor $A_{\tau,M}$ to obtain a time series of distance from the
 535 attractor $D_{\tau,M}(t)$.

536 From a time series of distances from the attractor, we estimated pathogen re-
 537 silience by fitting a linear regression to an appropriate window. To automatically
 538 select fitting windows, we began by smoothing the distance time series using locally
 539 estimated scatterplot smoothing (LOESS) to obtain $\hat{D}_{\tau,M}(t)$, where the smoothing
 540 is performed on a log scale and exponentiated afterwards. This smoothing allowed
 541 us to find appropriate threshold values for selecting fitting windows that are insensi-
 542 tive to errors in our estimates of distance from the attractor. Then, we determined
 543 threshold values (T_{start} and T_{end}) for the smoothed distances and choose the fitting
 544 window based on when $\hat{D}_{\tau,M}(t)$ crosses these threshold values for the first time.
 545 These thresholds were determined by first calculating the maximum distance,

$$\max \hat{D} = \max \hat{D}_{\tau,M}(t), \quad (3)$$

546 and the mean pre-pandemic distance,

$$\hat{D}_{\text{mean}} = \frac{1}{N_{t < 2020}} \sum_{t < 2020} \hat{D}_{\tau, M}(t), \quad (4)$$

547 as a reference, and then dividing their ratios into K equal bins,

$$T_{\text{start}} = \hat{D}_{\text{mean}} \times \left(\frac{\max \hat{D}}{\hat{D}_{\text{mean}}} \right)^{(K-a)/K}, \quad (5)$$

$$T_{\text{end}} = \hat{D}_{\text{mean}} \times \left(\frac{\max \hat{D}}{\hat{D}_{\text{mean}}} \right)^{a/K}, \quad (6)$$

548 where a represents the truncation threshold. This allows us to discard the initial
549 period during which the distance increases (from the introduction of intervention
550 measures) and the final period during which the distance plateaus (as the system
551 reaches an attractor). The fitting window is determined based on when the smoothed
552 distance $\hat{D}_{\tau, M}(t)$ crosses these threshold values for the first time; then, we fit a
553 linear regression to logged (unsmoothed) distances $\log D_{\tau, M}(t)$ using that window.
554 Alongside the threshold R for the false nearest neighbors approach, we tested optimal
555 choices for K and a values using simulations (Supplementary Text). We used $K = 19$
556 and $a = 2$ throughout the paper based on the simulation results.

557 Mathematical modeling

558 Throughout the paper, we use a series of mathematical models to illustrate the
559 concept of pathogen resilience and to understand the determinants of pathogen re-
560 silience. In general, the intrinsic resilience of a given system is given by the largest
561 real part of the eigenvalues of the linearized system at endemic equilibrium. Here, we
562 focus on the SIRS model with demography (birth and death) and present the details
563 of other models in Supplementary Text. The SIRS (Susceptible-Infected-Recovered-
564 Susceptible) model is the simplest model that allows for waning of immunity, where
565 recovered (immune) individuals are assumed to become fully susceptible after an
566 average of $1/\delta$ time period. The dynamics of the SIRS model is described by the
567 following set of differential equations:

$$\frac{dS}{dt} = \mu - \beta(t)SI - \mu S + \delta R \quad (7)$$

$$\frac{dI}{dt} = \beta(t)SI - (\gamma + \mu)I \quad (8)$$

$$\frac{dR}{dt} = \gamma I - (\delta + \mu)R \quad (9)$$

568 where μ represents the birth and death rates, $\beta(t)$ represents the time-varying trans-
569 mission rate, and γ represents the recovery rate. The basic reproduction number

570 $\mathcal{R}_0(t) = \beta(t)/(\gamma + \mu)$ is defined as the average number of secondary infections that
 571 a single infected individual would cause in a fully susceptible population at time t
 572 and measures the intrinsic transmissibility of a pathogen.

573 When we introduced the idea of pathogen resilience (Figure 2), we imposed sinu-
 574 soidal changes to the transmission rate to account for seasonal transmission,

$$\beta(t) = b_1(1 + \theta \cos(2\pi(t - \phi)))\alpha(t), \quad (10)$$

575 where b_1 represents the baseline transmission rate, θ represents the seasonal ampli-
 576 tude, and ϕ represents the seasonal offset term. Here, we also introduced an extra
 577 multiplicative term $\alpha(t)$ to account for the impact of pandemic perturbations, where
 578 $\alpha(t) < 1$ indicates transmission reduction. Figure 2A and 2B were generated assum-
 579 ing $b_1 = 3 \times (365/7 + 1/50)/\text{years}$, $\theta = 0.2$, $\phi = 0$, $\mu = 1/50/\text{years}$, $\gamma = 365/7/\text{years}$,
 580 and $\delta = 1/2/\text{years}$. Specifically, $b_1 = 3 \times (365/7 + 1/50)/\text{years}$ implies $\mathcal{R}_0 = 3$, where
 581 $(365/7 + 1/50)/\text{years}$ represent the rate of recovery. In Figure 2A, we imposed a 50%
 582 transmission reduction for 6 months from 2020:

$$\alpha(t) = \begin{cases} 0.5 & 2020 \leq t < 2020.5 \\ 1 & \text{otherwise} \end{cases} \quad (11)$$

583 In Figure 2B, we imposed a 50% transmission reduction for 6 months from 2020 and
 584 a permanent 10% reduction onward:

$$\alpha(t) = \begin{cases} 1 & t < 2020 \\ 0.5 & 2020 \leq t < 2020.5 \\ 0.9 & 2020.5 \leq t \end{cases} \quad (12)$$

585 In both scenarios, we simulated the SIRS model from the same initial conditions
 586 ($S(0) = 1/\mathcal{R}_0$, $I(0) = 1 \times 10^{-6}$, and $R(0) = 1 - S(0) - I(0)$) from 1900 until 2030.
 587 Throughout the paper, all deterministic models were solved using the **lsoda** solver
 588 from the **deSolve** package [44] in R [45].

589 To measure the empirical resilience of the SIRS model (Figure 2C and 2F), we
 590 computed the normalized distance between post-intervention susceptible and logged
 591 infected proportions and their corresponding unperturbed values at the same time:

$$\sqrt{\left(\frac{S(t) - S_{\text{unperturbed}}(t)}{\sigma_S}\right)^2 + \left(\frac{\log I(t) - \log I_{\text{unperturbed}}(t)}{\sigma_{\log I}}\right)^2}, \quad (13)$$

592 where σ_S and $\sigma_{\log I}$ represent the standard deviation in the unperturbed susceptible
 593 and logged infected proportions. The unperturbed values were obtained by simulat-
 594 ing the same SIRS model without pandemic perturbations ($\alpha = 1$). We normalized
 595 the differences in susceptible and logged infected proportions to allow both quantities
 596 to equally contribute to the changes in distance from the attractor. We used logged
 597 prevalence, instead of absolute prevalence, in order to capture epidemic dynamics

598 in deep troughs during the intervention period. In Supplementary Materials, we
 599 also compared how the degree of seasonal transmission affects empirical resilience
 600 by varying θ from 0 to 0.4; when we assumed no seasonality ($\theta = 0$), we did not
 601 normalize the distance because the standard deviation of pre-intervention dynamics
 602 are zero.

603 We used the SIRS model to understand how underlying epidemiological parameters
 604 affect pathogen resilience and determine the relationship to underlying sus-
 605 ceptible host dynamics. For the simple SIRS model without seasonal transmission
 606 ($\theta = 0$), the intrinsic resilience equals

$$-\frac{\text{Re}(\lambda)}{2} = \frac{\delta + \beta I^* + \mu}{2}. \quad (14)$$

607 Here, I^* represents the prevalence at endemic equilibrium:

$$I^* = \frac{(\delta + \mu)(\beta - (\gamma + \mu))}{\beta(\delta + \gamma + \mu)}. \quad (15)$$

608 The susceptible replenishment rate is given by

$$S_{\text{replenish}} = \frac{\mu + \delta R}{S^*}, \quad (16)$$

609 where $S^* = 1/\mathcal{R}_0$ represents the equilibrium proportion of susceptible individuals.
 610 We varied the basic reproduction number \mathcal{R}_0 between 1.1 to 6 and the average
 611 duration of immunity $1/\delta$ between 2 to 4 years, and computed these two quantities.
 612 In doing so, we fixed all other parameters: $\mu = 1/80/\text{years}$ and $\gamma = 365/7/\text{years}$.
 613 When infection provides a life-long immunity ($\delta = 0$), the intrinsic resilience is
 614 inversely proportional to the susceptible replenishment rate:

$$-\frac{\text{Re}(\lambda)}{2} = \frac{\mu}{2S^*} = \frac{S_{\text{replenish}}}{2}. \quad (17)$$

615 Finally, we used a seasonally unforced stochastic SIRS model without demog-
 616 raphy to understand how pathogen resilience affects sensitivity of the system to
 617 demographic stochasticity (see Supplementary Text for the details of the stochas-
 618 tic SIRS model). By varying the basic reproduction number \mathcal{R}_0 between 2 to 20
 619 and the average duration of immunity $1/\delta$ between 1 to 40 years, we ran the SIRS
 620 model for 100 years and computed the epidemic amplitude, which we defined as
 621 $(\max I - \min I)/(2\bar{I})$. Each simulation began from the equilibrium, and we trun-
 622 cated the initial 25 years before computing the epidemic amplitude. In doing so,
 623 we assumed $\gamma = 365/7/\text{years}$ and fixed the population size to 1 billion to prevent
 624 any fadeouts. We also considered a seasonally forced stochastic SIRS model without
 625 demography, assuming an amplitude of seasonal forcing of 0.04; in this case, we com-
 626 puted the relative epidemic amplitude by comparing the deterministic and stochastic
 627 trajectories (Supplementary Materials).

628 **Data availability**

629 All data and code are stored in a publicly available GitHub repository (<https://github.com/cobeylab/return-time>).
630

631 **Funding**

632 S.W.P. is a Peter and Carmen Lucia Buck Foundation Awardee of the Life Sciences
633 Research Foundation. S.C. was supported by Federal funds from the National Insti-
634 tute of Allergy and Infectious Diseases, National Institutes of Health, Department of
635 Health and Human Services under CEIRR contract 75N93021C00015. The content is
636 solely the responsibility of the authors and does not necessarily represent the official
637 views of the NIAID or the National Institutes of Health.

638 **Supplementary Text**

639 **Resilience of a stage-structured system.**

640 In Figure 2G–I, we used a more realistic, stage-structured model to illustrate how
 641 transient phenomena can cause the system to slow down. Specifically, we used the
 642 stage-structured RSV model proposed by [27], which assumes that subsequent rein-
 643 fections cause an individual to become less susceptible and transmissible than previ-
 644 ous infections. In contrast to a standard SIRS model, this model does not include a
 645 recovered compartment, which allow for temporary protection against new infections,
 646 and assumes that recovered individuals are immediately susceptible to new infections.
 647 The model dynamics can be described as follows:

$$\frac{dM}{dt} = \mu - (\omega + \mu)M \quad (S1)$$

$$\frac{dS_0}{dt} = \omega M - (\lambda(t) + \mu)S_0 \quad (S2)$$

$$\frac{dI_1}{dt} = \lambda(t)S_0 - (\gamma_1 + \mu)I_1 \quad (S3)$$

$$\frac{dS_1}{dt} = \gamma_1 I_1 - (\sigma_1 \lambda(t) + \mu)S_1 \quad (S4)$$

$$\frac{dI_2}{dt} = \sigma_1 \lambda(t)S_1 - (\gamma_2 + \mu)I_2 \quad (S5)$$

$$\frac{dS_2}{dt} = \gamma_2 I_2 - (\sigma_2 \lambda(t) + \mu)S_2 \quad (S6)$$

$$\frac{dI_3}{dt} = \sigma_2 \lambda(t)S_2 - (\gamma_3 + \mu)I_3 \quad (S7)$$

$$\frac{dS_3}{dt} = \gamma_3 I_3 - (\sigma_3 \lambda(t) + \mu)S_3 + \gamma_4 I_4 \quad (S8)$$

$$\frac{dI_4}{dt} = \sigma_3 \lambda(t)S_3 - (\gamma_4 + \mu)I_4 \quad (S9)$$

648 where M represents the proportion of individuals who are maternally immune; S_i
 649 represents the proportion of individuals who are susceptible after i prior infections; I_i
 650 represents the proportion of individuals who are currently (re)-infected with their i -th
 651 infection; μ represents the birth and death rates; $1/\omega$ represents the mean duration
 652 of maternal immunity; $1/\gamma_i$ represents the mean duration of infection; $\lambda(t)$ represents
 653 the force of infection; and σ_i represents the reduction in susceptibility for the i -th
 654 reinfection. The force of infection is modeled using a sinusoidal function:

$$\beta(t) = b_1(1 + \theta \cos(2\pi(t - \phi)))\alpha(t) \quad (S10)$$

$$\lambda(t) = \beta(I_1 + \rho_1 I_2 + \rho_2(I_3 + I_4)), \quad (S11)$$

655 where b_1 represents the baseline transmission rate; θ represents the seasonal ampli-
 656 tude; ϕ represents the seasonal offset term; $\alpha(t)$ represents the intervention effect;

and ρ_i represents the impact of immunity on transmission reduction. We used the following parameters to simulate the impact of interventions on epidemic dynamics [27]: $b_1 = 9 \times (365/10 + 1/80)/\text{years}$, $\theta = 0.2$, $\phi = -0.1$, $\omega = 365/112/\text{years}$, $\gamma_1 = 365/10/\text{years}$, $\gamma_2 = 365/7/\text{years}$, $\gamma_3 = 365/5/\text{years}$, $\sigma_1 = 0.76$, $\sigma_2 = 0.6$, $\sigma_3 = 0.4$, $\rho_1 = 0.75$, $\rho_2 = 0.51$, and $\mu = 1/80/\text{years}$. We assumed a 50% transmission reduction for 6 months from 2020:

$$\alpha(t) = \begin{cases} 0.5 & 2020 \leq t < 2020.5 \\ 1 & \text{otherwise} \end{cases} \quad (\text{S12})$$

The model was simulated from 1900 to 2030 using the following initial conditions: $M = 0$, $S_0 = 1/\mathcal{R}_0 - I_1$, $I_1 = 1 \times 10^{-6}$, $S_1 = 1 - 1/\mathcal{R}_0$, $I_2 = 0$, $S_2 = 0$, $I_3 = 0$, $S_3 = 0$, and $I_4 = 0$. For the phase plane analysis (Figure 2H) and distance analysis (Figure 2I), we relied on the average susceptibility,

$$\bar{S} = S_0 + \sigma_1 S_1 + \sigma_2 S_2 + \sigma_3 S_3, \quad (\text{S13})$$

and total prevalence,

$$I_{\text{total}} = I_1 + I_2 + I_3 + I_4. \quad (\text{S14})$$

These quantities were used to compute the normalized distance from the attractor, as described in the main text.

Resilience of a multistain system.

We used a simple two-strain model to show that a multistain host-pathogen system that is coupled through cross immunity can be described by a single resilience value. The model dynamics can be described as follows [35]:

$$\frac{dS}{dt} = \mu - \mu S - (\lambda_1 + \lambda_2)S + \delta_1 R_1 + \delta_2 R_2 \quad (\text{S15})$$

$$\frac{dI_1}{dt} = \lambda_1 S - (\gamma_1 + \mu)I_1 \quad (\text{S16})$$

$$\frac{dI_2}{dt} = \lambda_2 S - (\gamma_2 + \mu)I_2 \quad (\text{S17})$$

$$\frac{dR_1}{dt} = \gamma_1 I_1 - \lambda_2 \epsilon_{21} R_1 - \delta_1 R_1 + \delta_2 R - \mu R_1 \quad (\text{S18})$$

$$\frac{dR_2}{dt} = \gamma_2 I_2 - \lambda_1 \epsilon_{12} R_2 - \delta_2 R_2 + \delta_1 R - \mu R_2 \quad (\text{S19})$$

$$\frac{dJ_1}{dt} = \lambda_1 \epsilon_{12} R_2 - (\gamma_1 + \mu) J_1 \quad (\text{S20})$$

$$\frac{dJ_2}{dt} = \lambda_2 \epsilon_{21} R_1 - (\gamma_2 + \mu) J_2 \quad (\text{S21})$$

$$\frac{dR}{dt} = \gamma_1 J_1 + \gamma_2 J_2 - \delta_1 R - \delta_2 R - \mu R \quad (\text{S22})$$

where S represents the proportion of individuals who are fully susceptible to infections by both strains; I_1 represents the proportion of individuals who are infected with strain 1 without prior immunity; I_2 represents the proportion of individuals who are infected with strain 2 without prior immunity; R_1 represents the proportion of individuals who are fully immune against strain 1 and partially susceptible to reinfection by strain 2; R_2 represents the proportion of individuals who are fully immune against strain 2 and partially susceptible to reinfection by strain 1; J_1 represents the proportion of individuals who are infected with strain 1 with prior immunity against strain 2; J_2 represents the proportion of individuals who are infected with strain 2 with prior immunity against strain 1; R represents the proportion of individuals who are immune to infections from both strains; μ represents the birth/death rate; λ_1 and λ_2 represent the force of infection from strains 1 and 2, respectively; δ_1 and δ_2 represent the waning immunity rate; γ_1 and γ_2 represent the recovery rate; ϵ_{21} and ϵ_{12} represent the susceptibility to reinfection with strains 2 and 1, respectively, given prior immunity from infection with strains 1 and 2, respectively. The force of infection is modeled as follows:

$$\beta_1 = b_1(1 + \theta_1 \sin(2\pi(t - \phi_1)))\alpha(t) \quad (\text{S23})$$

$$\beta_2 = b_2(1 + \theta_2 \sin(2\pi(t - \phi_2)))\alpha(t) \quad (\text{S24})$$

$$\lambda_1 = \beta_1(I_1 + J_1) \quad (\text{S25})$$

$$\lambda_2 = \beta_2(I_2 + J_2) \quad (\text{S26})$$

In Supplementary Figures S2–S4, we assumed the following parameters: $b_1 = 2 \times 52/\text{years}$, $b_2 = 4 \times 52/\text{years}$, $\phi_1 = \phi_2 = 0$, $\epsilon_{12} = 0.9$, $\epsilon_{21} = 0.5$, $\gamma_1 = \gamma_2 = 52/\text{years}$, $\delta_1 = \delta_2 = 1/\text{years}$, and $\mu = 1/70/\text{years}$. For all simulations, we assumed a 50% transmission reduction for 6 months from 2020:

$$\alpha(t) = \begin{cases} 0.5 & 2020 \leq t < 2020.5 \\ 1 & \text{otherwise} \end{cases} \quad (\text{S27})$$

The seasonal amplitude θ is varied from 0 to 0.4. All simulations were run from 1900 to 2030 with following initial conditions: $S(0) = 1 - 2 \times 10^{-6}$, $I_1(0) = 1 \times 10^{-6}$, $I_2(0) = 1 \times 10^{-6}$, $R_1(0) = 0$, $R_2(0) = 0$, $J_1(0) = 0$, $J_2(0) = 0$, and $R(0) = 0$.

We considered three scenarios for measuring pathogen resilience: (1) we only have information about strain 1, (2) we only have information about strain 2, and (3) we are unable to distinguish between strains. In the first two scenarios (see panels A–C for strain 1 and panels D–F for strain 2), we considered the dynamics of average susceptibility for each strain and total prevalence:

$$\bar{S}_1 = S + \epsilon_{12}R_2 \quad (\text{S28})$$

$$\hat{I}_1 = I_1 + J_1 \quad (\text{S29})$$

$$\bar{S}_2 = S + \epsilon_{21}R_1 \quad (\text{S30})$$

$$\hat{I}_2 = I_2 + J_2 \quad (\text{S31})$$

⁷⁰² In the third scenario (panels G–I), we considered the dynamics of total susceptible
⁷⁰³ and infected populations:

$$\hat{S} = S + R_2 + R_1 \quad (\text{S32})$$

$$\hat{I} = I_1 + J_1 + I_2 + J_2 \quad (\text{S33})$$

⁷⁰⁴ These quantities were used to compute the normalized distance from the attractor,
⁷⁰⁵ as described in the main text.

⁷⁰⁶ Estimating intrinsic resilience using a mechanistic model

⁷⁰⁷ We tested whether we can reliably estimate the intrinsic resilience of a system by fit-
⁷⁰⁸ ting a mechanistic model. Specifically, we simulated case time series from stochastic
⁷⁰⁹ SIRS and two-strain models and fitted a simple, deterministic SIRS model using a
⁷¹⁰ Bayesian framework [4, 24, 46].

⁷¹¹ We simulated the models in discrete time with a daily time step ($\Delta t = 1$),
⁷¹² incorporating demographic stochasticity:

$$\beta(t) = \mathcal{R}_0 \left(1 + \theta \cos \left(\frac{2\pi t}{364} \right) \right) \alpha(t)(1 - \exp(-\gamma)) \quad (\text{S34})$$

$$\text{FOI}(t) = \beta(t)I(t - \Delta t)/N \quad (\text{S35})$$

$$B(t) \sim \text{Poisson}(\mu N) \quad (\text{S36})$$

$$\Delta S(t) \sim \text{Binom}(S(t - \Delta t), 1 - \exp(-(\text{FOI}(t) + \mu)\Delta t)) \quad (\text{S37})$$

$$N_{SI}(t) \sim \text{Binom}\left(\Delta S(t), \frac{\text{FOI}(t)}{\text{FOI}(t) + \mu}\right) \quad (\text{S38})$$

$$\Delta I(t) \sim \text{Binom}(I(t - \Delta t), 1 - \exp(-(\gamma + \mu)\Delta t)) \quad (\text{S39})$$

$$N_{IR}(t) \sim \text{Binom}\left(\Delta I(t), \frac{\gamma}{\gamma + \mu}\right) \quad (\text{S40})$$

$$\Delta R(t) \sim \text{Binom}(R(t - \Delta t), 1 - \exp(-(\delta + \mu)\Delta t)) \quad (\text{S41})$$

$$N_{RS}(t) \sim \text{Binom}\left(\Delta R(t), \frac{\delta}{\delta + \mu}\right) \quad (\text{S42})$$

$$S(t) = S(t - \Delta t) + N_{RS}(t) + B(t) - \Delta S(t) \quad (\text{S43})$$

$$I(t) = I(t - \Delta t) + N_{SI}(t) - \Delta I(t) \quad (\text{S44})$$

$$R(t) = R(t - \Delta t) + N_{IR}(t) - \Delta R(t) \quad (\text{S45})$$

⁷¹³ where FOI represents the force of infection; N_{ij} represents the number of individuals
⁷¹⁴ moving from compartment i to j on a given day; and $B(t)$ represents the number
⁷¹⁵ of new births. All other parameters definitions can be found in the description of
⁷¹⁶ the deterministic version of the model. We simulated the model on a daily scale—
⁷¹⁷ assuming 364 days in a year so that it can be evenly grouped into 52 weeks—with
⁷¹⁸ the following parameters: $\mathcal{R}_0 = 3$, $\theta = 0.1$, $\gamma = 1/7/\text{days}$, $\delta = 1/(364 \times 2)/\text{days}$,

⁷¹⁹ $\mu = 1/(364 \times 50)/\text{days}$, and $N = 1 \times 10^8$. The model was simulated from 1900 to
⁷²⁰ 2030 assuming $S(0) = N/3$, $I(0) = 100$, and $R(0) = N - S(0) - I(0)$. The observed
⁷²¹ incidence from the model was then simulated as follows:

$$C(t) = \text{Beta-Binom}(N_{SI}(t), \rho, k), \quad (\text{S46})$$

⁷²² where ρ represents the reporting probability and k represents the overdispersion
⁷²³ parameter of beta-binomial distribution. Here, we used the beta-binomial distribu-
⁷²⁴ tion to account for overdispersion in reporting. We assumed $\rho = 0.002$ (i.e., 0.2%
⁷²⁵ probability) and $k = 1000$.

⁷²⁶ We used an analogous approach for the two-strain model:

$$\beta_1(t) = b_1 \left(1 + \theta_1 \cos \left(\frac{2\pi(t - \phi_1)}{364} \right) \right) \alpha(t) \quad (\text{S47})$$

$$\beta_2(t) = b_2 \left(1 + \theta_2 \cos \left(\frac{2\pi(t - \phi_2)}{364} \right) \right) \alpha(t) \quad (\text{S48})$$

$$\text{FOI}_1(t) = \beta_1(t)(I_1(t - \Delta t) + J_1(t - \Delta t))/N \quad (\text{S49})$$

$$\text{FOI}_2(t) = \beta_2(t)(I_2(t - \Delta t) + J_2(t - \Delta t))/N \quad (\text{S50})$$

$$B(t) \sim \text{Poisson}(\mu N) \quad (\text{S51})$$

$$\Delta S(t) \sim \text{Binom}(S(t - \Delta t), 1 - \exp(-(\text{FOI}_1(t) + \text{FOI}_2(t) + \mu)\Delta t)) \quad (\text{S52})$$

$$N_{SI_1}(t) \sim \text{Binom}\left(\Delta S(t), \frac{\text{FOI}_1(t)}{\text{FOI}_1(t) + \text{FOI}_2(t) + \mu}\right) \quad (\text{S53})$$

$$N_{SI_2}(t) \sim \text{Binom}\left(\Delta S(t), \frac{\text{FOI}_2(t)}{\text{FOI}_1(t) + \text{FOI}_2(t) + \mu}\right) \quad (\text{S54})$$

$$\Delta I_1(t) \sim \text{Binom}(I_1(t - \Delta t), 1 - \exp(-(\gamma_1 + \mu)\Delta t)) \quad (\text{S55})$$

$$N_{I_1 R_1}(t) \sim \text{Binom}\left(\Delta I_1(t), \frac{\gamma_1}{\gamma_1 + \mu}\right) \quad (\text{S56})$$

$$\Delta I_2(t) \sim \text{Binom}(I_2(t - \Delta t), 1 - \exp(-(\gamma_2 + \mu)\Delta t)) \quad (\text{S57})$$

$$N_{I_2 R_2}(t) \sim \text{Binom}\left(\Delta I_2(t), \frac{\gamma_2}{\gamma_2 + \mu}\right) \quad (\text{S58})$$

$$\Delta R_1(t) \sim \text{Binom}(R_1(t - \Delta t), 1 - \exp(-(\epsilon_{21}\text{FOI}_2(t) + \rho_1 + \mu)\Delta t)) \quad (\text{S59})$$

$$N_{R_1 S}(t) \sim \text{Binom}\left(\Delta R_1(t), \frac{\rho_1}{\epsilon_{21}\text{FOI}_2(t) + \rho_1 + \mu}\right) \quad (\text{S60})$$

$$N_{R_1 J_2}(t) \sim \text{Binom}\left(\Delta R_1(t), \frac{\epsilon_{21}\text{FOI}_2(t)}{\epsilon_{21}\text{FOI}_2(t) + \rho_1 + \mu}\right) \quad (\text{S61})$$

$$\Delta R_2(t) \sim \text{Binom}(R_2(t - \Delta t), 1 - \exp(-(\epsilon_{12}\text{FOI}_1(t) + \rho_2 + \mu)\Delta t)) \quad (\text{S62})$$

$$N_{R_2 S}(t) \sim \text{Binom}\left(\Delta R_2(t), \frac{\rho_2}{\epsilon_{12}\text{FOI}_1(t) + \rho_2 + \mu}\right) \quad (\text{S63})$$

$$N_{R_2 J_1}(t) \sim \text{Binom}\left(\Delta R_2(t), \frac{\epsilon_{12}\text{FOI}_1(t)}{\epsilon_{12}\text{FOI}_1(t) + \rho_2 + \mu}\right) \quad (\text{S64})$$

$$\Delta J_1(t) \sim \text{Binom}(J_1(t - \Delta t), 1 - \exp(-(\gamma_1 + \mu)\Delta t)) \quad (\text{S65})$$

$$N_{J_1R}(t) \sim \text{Binom}\left(\Delta J_1(t), \frac{\gamma_1}{\gamma_1 + \mu}\right) \quad (\text{S66})$$

$$\Delta J_2(t) \sim \text{Binom}(J_2(t - \Delta t), 1 - \exp(-(\gamma_2 + \mu)\Delta t)) \quad (\text{S67})$$

$$N_{J_2R}(t) \sim \text{Binom}\left(\Delta J_2(t), \frac{\gamma_2}{\gamma_2 + \mu}\right) \quad (\text{S68})$$

$$\Delta R(t) \sim \text{Binom}(R(t - \Delta t), 1 - \exp(-(\rho_1 + \rho_2 + \mu)\Delta t)) \quad (\text{S69})$$

$$N_{RR_1}(t) \sim \text{Binom}\left(\Delta R(t), \frac{\rho_1}{\rho_1 + \rho_2 + \mu}\right) \quad (\text{S70})$$

$$N_{RR_2}(t) \sim \text{Binom}\left(\Delta R(t), \frac{\rho_2}{\rho_1 + \rho_2 + \mu}\right) \quad (\text{S71})$$

$$S(t) = S(t - \Delta t) - \Delta S(t) + B(t) + N_{R_1S}(t) + N_{R_2S}(t) \quad (\text{S72})$$

$$I_1(t) = I_1(t - \Delta t) - \Delta I_1(t) + N_{SI_1}(t) \quad (\text{S73})$$

$$I_2(t) = I_2(t - \Delta t) - \Delta I_2(t) + N_{SI_2}(t) \quad (\text{S74})$$

$$R_1(t) = R_1(t - \Delta t) - \Delta R_1(t) + N_{I_1R_1}(t) + N_{RR_1}(t) \quad (\text{S75})$$

$$R_2(t) = R_2(t - \Delta t) - \Delta R_2(t) + N_{I_2R_2}(t) + N_{RR_2}(t) \quad (\text{S76})$$

$$J_1(t) = J_1(t - \Delta t) - \Delta J_1(t) + N_{R_2J_1}(t) \quad (\text{S77})$$

$$J_2(t) = J_2(t - \Delta t) - \Delta J_2(t) + N_{R_1J_2}(t) \quad (\text{S78})$$

$$R(t) = R(t - \Delta t) - \Delta R(t) + N_{J_1R}(t) + N_{J_2R}(t) \quad (\text{S79})$$

We simulated the model on a daily scale with previously estimated parameters for the RSV-HMPV interaction [35]: $b_1 = 1.7/\text{weeks}$, $b_2 = 1.95/\text{weeks}$, $\theta_1 = 0.4$, $\theta_2 = 0.3$, $\phi_1 = 0.005 \times 7/364$, $\phi_2 = 4.99 \times 7/364$, $\epsilon_{12} = 0.92$, $\epsilon_{21} = 0.45$, $\gamma_1 = 1/10/\text{days}$, $\gamma_2 = 1/10/\text{days}$, $\rho_1 = 1/364/\text{days}$, $\rho_2 = 1/364/\text{days}$, $\mu = 1/(70 \times 364)/\text{days}$, and $N = 1 \times 10^8$. The model was simulated from 1900 to 2030 assuming $S(0) = N - 200$, $I_1(0) = 100$, $I_2(0) = 100$, $R_1(0) = 0$, $R_2(0) = 0$, $J_1(0) = 0$, $J_2(0) = 0$, and $R(0) = 0$. The observed incidence for each strain is then simulated as follows:

$$C_1(t) = \text{Beta-Binom}(N_{SI_1}(t) + N_{R_2J_1}, \rho, k), \quad (\text{S80})$$

$$C_2(t) = \text{Beta-Binom}(N_{SI_2}(t) + N_{R_1J_2}, \rho, k), \quad (\text{S81})$$

where ρ represents the reporting probability and k represents the overdispersion parameter of beta-binomial distribution. We assumed $\rho = 0.002$ (i.e., 0.2% probability) and $k = 500$. We also considered the total incidence: $C_{\text{total}}(t) = C_1(t) + C_2(t)$.

For both models, we considered a more realistically shaped pandemic perturbation $\alpha(t)$ to challenge our ability to estimate the intervention effects. Thus, we assumed a 40% transmission reduction for 3 months from March 2020, followed by a 10% transmission reduction for 6 months, 20% transmission reduction for 3 months,

⁷⁴¹ and a final return to normal levels:

$$\alpha(t) = \begin{cases} 1 & t < 2020.25 \\ 0.6 & 2020.25 \leq t < 2020.5 \\ 0.9 & 2020.5 \leq t < 2021 \\ 0.8 & 2021 \leq t < 2021.25 \\ 1 & 2021.25 \leq t \end{cases}. \quad (\text{S82})$$

⁷⁴² For all simulations, we truncated the time series from the beginning of 2014 to the
⁷⁴³ end of 2023 and aggregated them into weekly cases.

⁷⁴⁴ To infer intrinsic resilience from time series, we fitted a simple discrete time,
⁷⁴⁵ deterministic SIRS model in a Bayesian framework [4]:

$$\Delta t = 1 \text{ week} \quad (\text{S83})$$

$$\text{FOI}(t) = \beta(t)(I(t - \Delta t) + \omega)/N \quad (\text{S84})$$

$$\Delta S(t) = [1 - \exp(-(\text{FOI}(t) + \mu)\Delta t)] S(t - \Delta t) \quad (\text{S85})$$

$$N_{SI}(t) = \frac{\text{FOI}(t)\Delta S(t)}{\text{FOI}(t) + \mu} \quad (\text{S86})$$

$$\Delta I(t) = [1 - \exp(-(\gamma + \mu)\Delta t)] I(t - \Delta t) \quad (\text{S87})$$

$$N_{IR}(t) = \frac{\gamma \Delta I(t)}{\gamma + \mu} \quad (\text{S88})$$

$$\Delta R(t) = [1 - \exp(-(\nu + \mu)\Delta t)] R(t - \Delta t) \quad (\text{S89})$$

$$N_{RS}(t) = \frac{\nu \Delta R(t)}{\nu + \mu} \quad (\text{S90})$$

$$S(t) = S(t - \Delta t) + \mu S - \Delta S(t) + N_{RS}(t) \quad (\text{S91})$$

$$I(t) = I(t - \Delta t) - \Delta I(t) + N_{SI}(t) \quad (\text{S92})$$

$$R(t) = R(t - \Delta t) - \Delta R(t) + N_{IR}(t) \quad (\text{S93})$$

⁷⁴⁶ where we include an extra term ω to account for importation. Although actual
⁷⁴⁷ simulations did not include any importation, we had found that including this term
⁷⁴⁸ generally helped with model convergence in previous analyses [4]. The transmission
⁷⁴⁹ rate was divided into a seasonal term $\beta_{\text{seas}}(t)$ (repeated every year) and intervention
⁷⁵⁰ term $\alpha(t)$, which were estimated jointly:

$$\beta(t) = \beta_{\text{seas}}(t)\alpha(t), \quad (\text{S94})$$

⁷⁵¹ where $\alpha < 1$ corresponds to reduction in transmission due to intervention effects. To
⁷⁵² constrain the smoothness of $\beta_{\text{seas}}(t)$, we imposed cyclic, random-walk priors:

$$\beta_{\text{seas}}(t) \sim \text{Normal}(\beta_{\text{seas}}(t - 1), \sigma) \quad t = 2 \dots 52 \quad (\text{S95})$$

$$\beta_{\text{seas}}(1) \sim \text{Normal}(\beta_{\text{seas}}(52), \sigma) \quad (\text{S96})$$

$$\sigma \sim \text{Half-Normal}(0, 1) \quad (\text{S97})$$

⁷⁵³ We fixed $\alpha(t) = 1$ for all $t < 2020$ and estimate α assuming a normal prior:

$$\alpha \sim \text{Normal}(1, 0.25). \quad (\text{S98})$$

⁷⁵⁴ We assumed weakly informative priors on ω and ν :

$$\omega \sim \text{Half-Normal}(0, 200) \quad (\text{S99})$$

$$\nu \sim \text{Normal}(104, 26) \quad (\text{S100})$$

⁷⁵⁵ We assumed that the true birth/death rates, population sizes, and recovery rates
⁷⁵⁶ are known. We note, however, that assuming $\gamma = 1/\text{week}$ actually corresponds to
⁷⁵⁷ a mean simulated infectious period of 1.6 weeks due to a time discretization, which
⁷⁵⁸ is much longer than the true value; this approximation allows us to test whether we
⁷⁵⁹ can still robustly estimate the intrinsic resilience given parameter mis-specification.
⁷⁶⁰ Initial conditions were estimated with following priors:

$$S(0) = Ns(0) \quad (\text{S101})$$

$$I(0) = Ni(0) \quad (\text{S102})$$

$$s(0) \sim \text{Uniform}(0, 1) \quad (\text{S103})$$

$$i(0) \sim \text{Half-Normal}(0, 0.001) \quad (\text{S104})$$

⁷⁶¹ Finally, the observation model was specified as follows:

$$\text{Cases}(t) \sim \text{Negative-Binomial}(\rho N_{SI}(t), \phi) \quad (\text{S105})$$

$$\rho \sim \text{Half-Normal}(0, 0.02) \quad (\text{S106})$$

$$\phi \sim \text{Half-Normal}(0, 10) \quad (\text{S107})$$

⁷⁶² where ρ represents the reporting probability and ϕ represents the negative binomial
⁷⁶³ overdispersion parameter.

⁷⁶⁴ The model was fitted to four separate time series: (1) incidence time series from
⁷⁶⁵ the SIRS model, (2) incidence time series for strain 1 from the two-strain model,
⁷⁶⁶ (3) incidence time series for strain 2 from the two-strain model, and (4) combined
⁷⁶⁷ incidence time series for strains 1 and 2 from the two-strain model. The model
⁷⁶⁸ was fitted using rstan [47, 48] with 4 chains, each consisting of 2000 iterations.
⁷⁶⁹ The resulting posterior distribution was used to calculate the intrinsic resilience of
⁷⁷⁰ the seasonally unforced SIRS model with the same parameters; eigenvalues of the
⁷⁷¹ discrete-time SIR model were computed by numerically finding the equilibrium and
⁷⁷² calculating the Jacobian matrix.

⁷⁷³ **Validations for window-selection criteria**

⁷⁷⁴ We used stochastic SIRS simulations to identify optimal parameters for the window-
⁷⁷⁵ selection criteria that we used for the linear regression for estimating empirical re-
⁷⁷⁶ silience. For each simulation, we began by generating a random perturbation $\alpha(t)$

777 from a random set of parameters. First, we drew the duration of perturbation τ_{npi}
 778 from a uniform distribution between 1 and 2 years. Then, we drew independent
 779 normal variables z_i of length $\lfloor 364\tau_{\text{npi}} \rfloor$ with a standard deviation of 0.02 and took a
 780 reverse cumulative sum to obtain a realistic shape for the perturbation:

$$x_n = 1 + \sum_{i=n}^{\lfloor 364\tau_{\text{npi}} \rfloor} z_i, \quad n = 1, \dots, \lfloor 364\tau_{\text{npi}} \rfloor. \quad (\text{S108})$$

781 In contrast to simple perturbations that assume a constant reduction in transmission,
 782 this approach allows us to model transmission reduction that varies over time
 783 smoothly. We repeated this random generation process until less than 10% of x_n
 784 exceeds 1—this was done to ensure the perturbation term $\alpha(t)$ stays below 1 (and
 785 therefore reduce transmission) for the most part. Then, we set any values that are
 786 above 1 or below 0 to 1 and 0, respectively. Then, we randomly drew the minimum
 787 transmission during perturbation α_{\min} from a uniform distribution between 0.5 and
 788 0.7 and scale x_n to have a minimum of α_{\min} :

$$x_{\text{scale},n} = \alpha_{\min} + (1 - \alpha_{\min}) \times \frac{x_n - \min x_n}{1 - \min x_n}. \quad (\text{S109})$$

789 This allowed us to simulate a realistically shaped perturbation:

$$\alpha(t) = \begin{cases} 1 & t < 2020 \\ x_{\text{scale},364(t-2020)} & 2020 \leq t < 2020 + \tau_{\text{npi}} \\ 1 & \tau_{\text{npi}} \leq t \end{cases}. \quad (\text{S110})$$

790 Given this perturbation function, we draw \mathcal{R}_0 from a uniform distribution between
 791 1.5 and 4 and the mean duration of immunity $1/\delta$ from a uniform distribution be-
 792 tween 1 and 4. Then, we simulate the stochastic SIRS model from $S(0) = 10^8/\mathcal{R}_0$
 793 and $I(0) = 100$ from 1990 to 2025 and truncate the time series to 2014–2025; if the
 794 epidemic becomes extinct before the end of simulation, we discard that simulation
 795 and start over from the perturbation generation step.

796 For each epidemic simulation, we computed the empirical resilience by varying
 797 the threshold R for the nearest neighbor approach from 4 to 14 with increments of
 798 2, the number of divisions K for the window selection between 8 and 25, and the
 799 truncation threshold a for the window selection between 1 to 3; this was done for all
 800 possible combinations of R , K , and a . We also compared this with the naive approach
 801 that uses the entire distance-from-attractor time series, starting from the maximum
 802 distance to the end of the time series. We repeated this procedure 500 times and
 803 quantified the correlation between empirical and intrinsic resilience estimates across
 804 two approaches.

Supplementary Figures

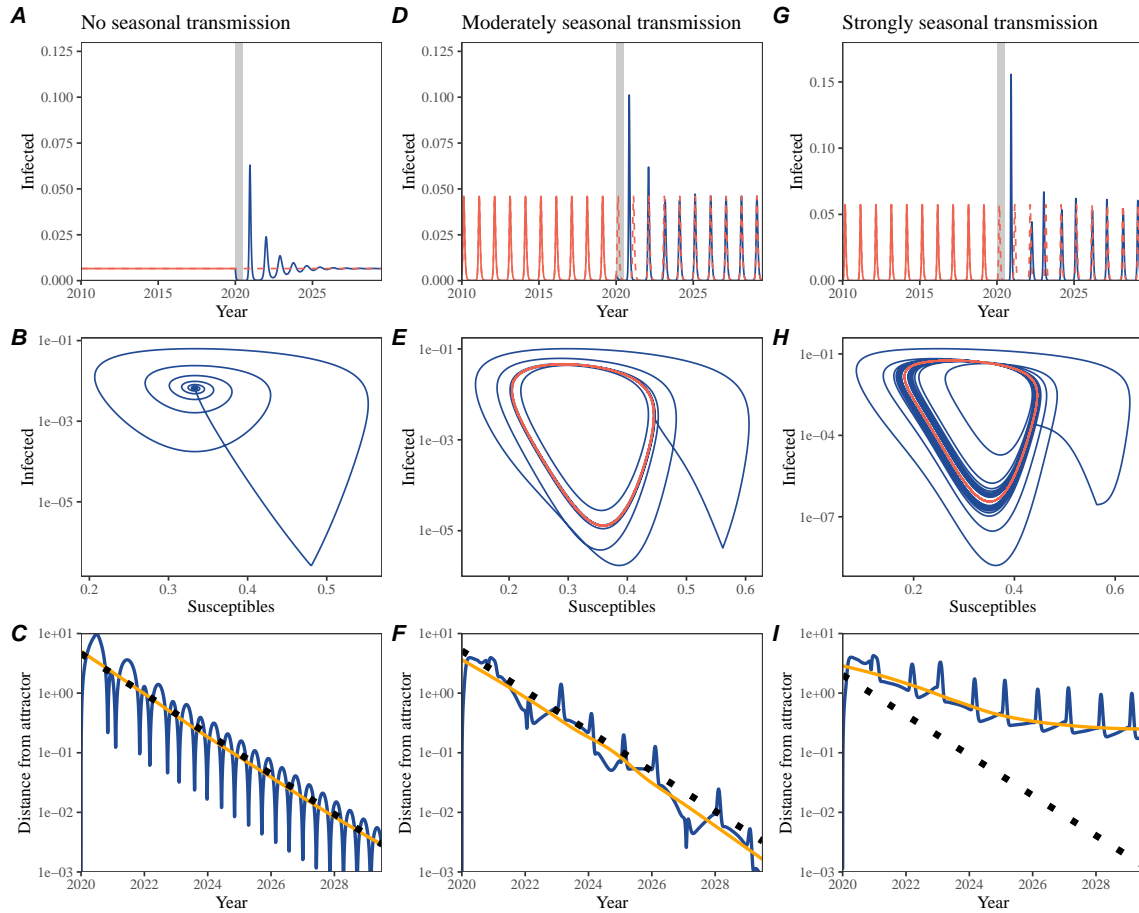


Figure S1: Impact of seasonal transmission on pathogen resilience. (A, D, G) Simulated epidemic trajectories using the SIRS model without seasonal forcing (A), with seasonal forcing of amplitude of 0.2 (D), and with seasonal forcing of amplitude of 0.4 (G). Red and blue solid lines represent epidemic dynamics before and after interventions are introduced, respectively. Red dashed lines represent counterfactual epidemic dynamics in the absence of interventions. Gray regions indicate the duration of interventions. (B, E, H) Phase plane representation of the time series in panels A, D, and G alongside the corresponding susceptible host dynamics. Red and blue solid lines represent epidemic trajectories on an SI phase plane before and after interventions are introduced, respectively. (C, F, I) Changes in logged distance from the attractor over time. Blue lines represent the logged distance from the attractor. Orange lines represent the locally estimated scatterplot smoothing (LOESS) fits to the logged distance from the attractor. Dotted lines show the intrinsic resilience of the seasonally unforced system.

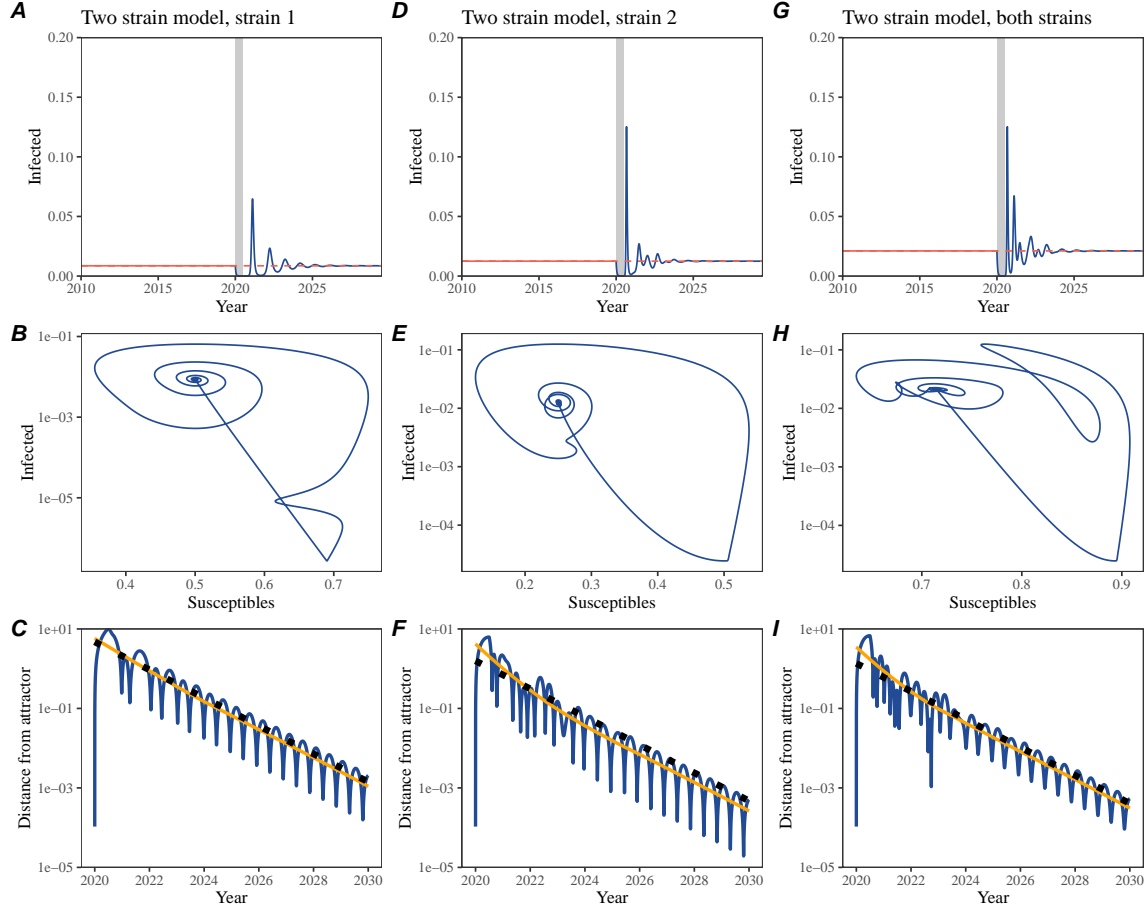


Figure S2: A simple method to measure pathogen resilience following pandemic perturbations for a two-strain competition system without seasonal forcing. (A, D, G) Simulated epidemic trajectories using a two-strain system without seasonal forcing. In this model, two strains compete through cross immunity. Red and blue solid lines represent epidemic dynamics before and after interventions are introduced, respectively. Red dashed lines represent counterfactual epidemic dynamics in the absence of interventions. Gray regions indicate the duration of interventions. (B, E, H) Phase plane representation of the time series in panels A, D, and G alongside the corresponding susceptible host dynamics. Blue solid lines represent epidemic trajectories on an SI phase plane before and after interventions. (C, F, I) Changes in logged distance from the attractor over time. Blue lines represent the logged distance from the attractor. Orange lines represent the locally estimated scatterplot smoothing (LOESS) fits to the logged distance from the attractor. Dotted lines show the intrinsic resilience of the seasonally unforced system.

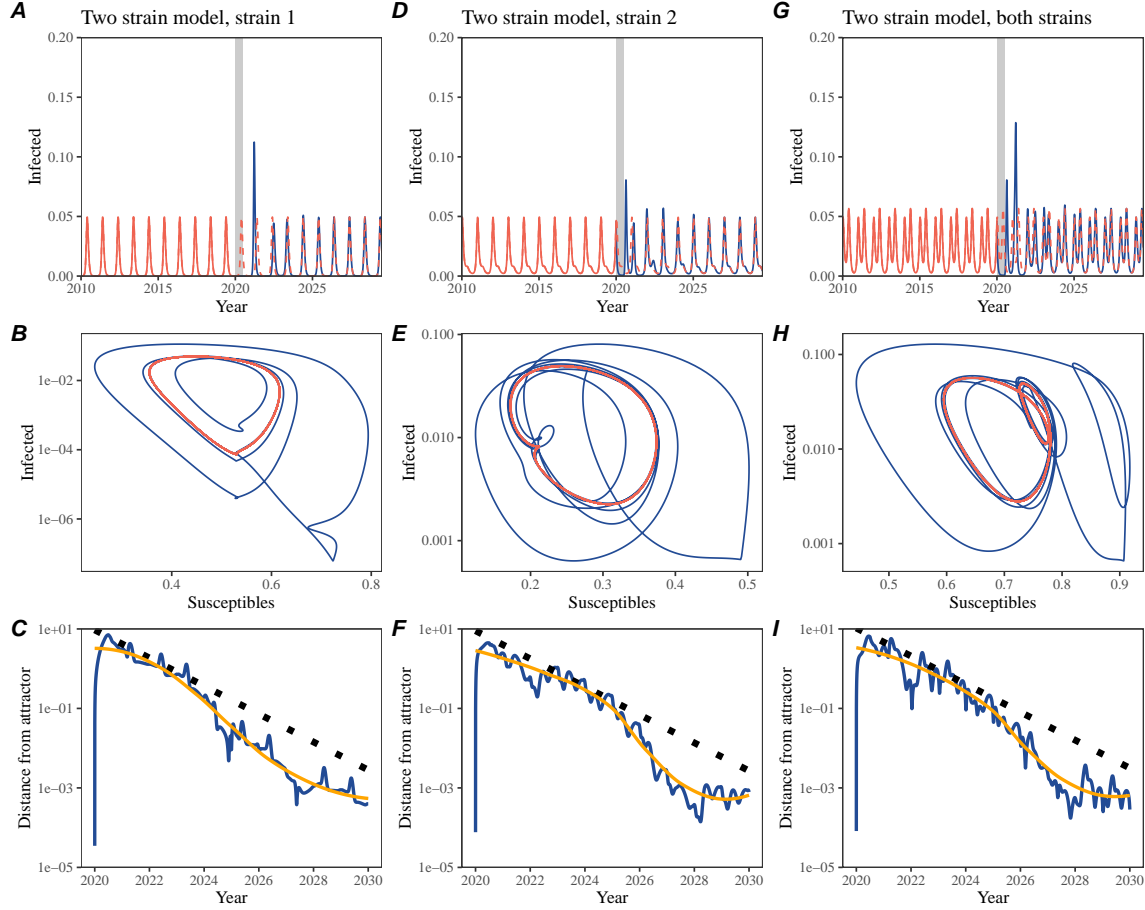


Figure S3: A simple method to measure pathogen resilience following pandemic perturbations for a two-strain competition system with seasonal forcing. (A, D, G) Simulated epidemic trajectories using a two-strain system with seasonal forcing (amplitude of 0.2). In this model, two strains compete through cross immunity. Red and blue solid lines represent epidemic dynamics before and after interventions are introduced, respectively. Red dashed lines represent counterfactual epidemic dynamics in the absence of interventions. Gray regions indicate the duration of interventions. (B, E, H) Phase plane representation of the time series in panels A, D, and G alongside the corresponding susceptible host dynamics. Red and blue solid lines represent epidemic trajectories on an SI phase plane before and after interventions are introduced, respectively. (C, F, I) Changes in logged distance from the attractor over time. Blue lines represent the logged distance from the attractor. Orange lines represent the locally estimated scatterplot smoothing (LOESS) fits to the logged distance from the attractor. Dotted lines show the intrinsic resilience of the seasonally unforced system.

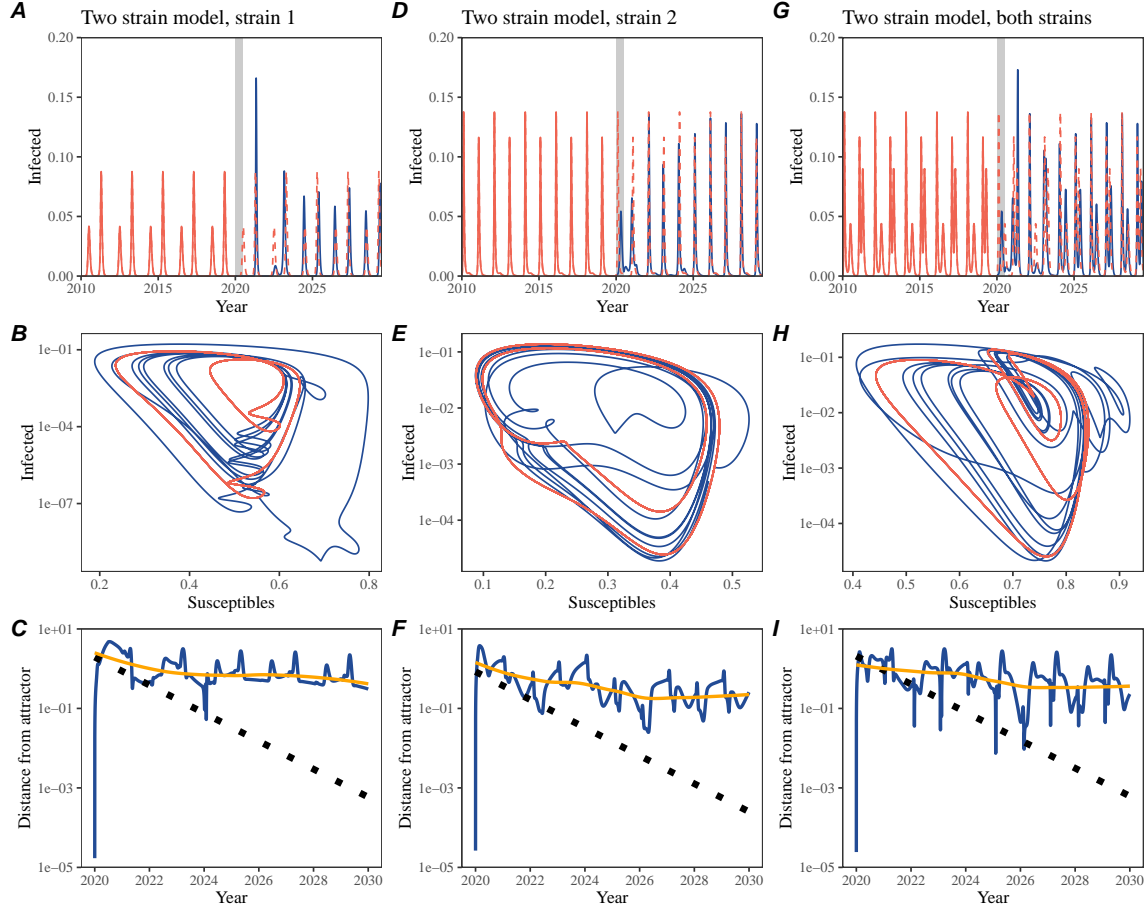


Figure S4: A simple method to measure pathogen resilience following pandemic perturbations for a multi-strain competition system with strong seasonal forcing. (A, D, G) Simulated epidemic trajectories using a two-strain system with seasonal forcing (amplitude of 0.2). In this model, two strains compete through cross immunity. Red and blue solid lines represent epidemic dynamics before and after interventions are introduced, respectively. Red dashed lines represent counterfactual epidemic dynamics in the absence of interventions. Gray regions indicate the duration of interventions. (B, E, H) Phase plane representation of the time series in panels A, D, and G alongside the corresponding susceptible host dynamics. Red and blue solid lines represent epidemic trajectories on an SI phase plane before and after interventions are introduced, respectively. (C, F, I) Changes in logged distance from the attractor over time. Blue lines represent the logged distance from the attractor. Orange lines represent the locally estimated scatterplot smoothing (LOESS) fits to the logged distance from the attractor. Dotted lines show the intrinsic resilience of the seasonally unforced system.

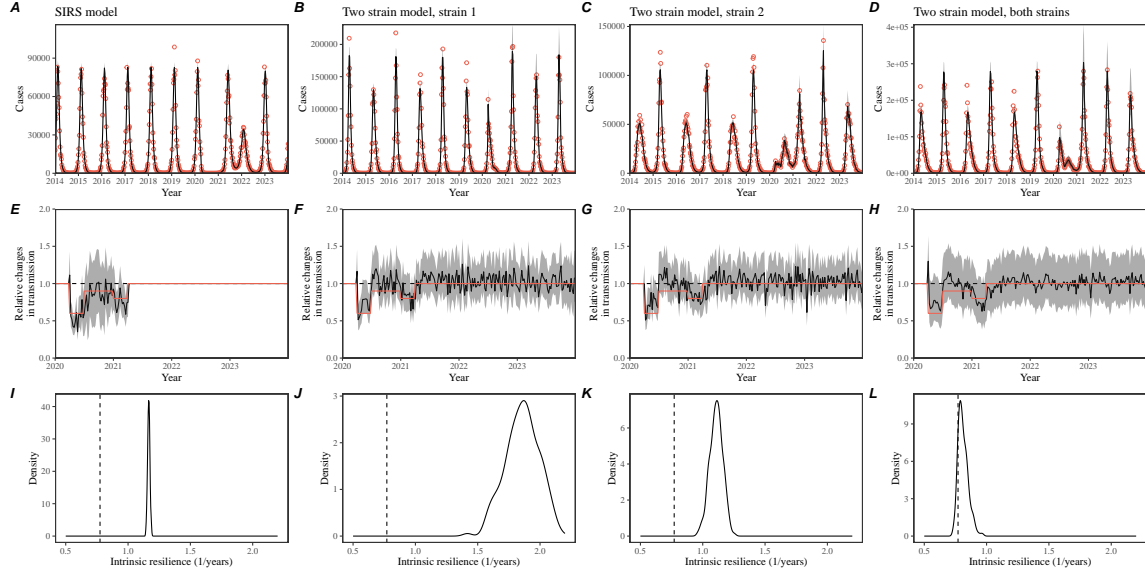


Figure S5: Mechanistic model fits to simulated data and inferred intrinsic resilience. We simulated discrete time, stochastic epidemic trajectories using a seasonally forced SIRS model (A,E,I) and a seasonally forced two-strain model (B–D, F–H, and J–L) and tested whether we can estimate the intrinsic resilience of the seasonally unforced versions of the model by fitting a mechanistic model (Supplementary Text). We fitted the same discrete time, one strain, deterministic SIRS model in each scenario. (A–D) Simulated case time series from corresponding models shown in the title (red) and SIRS model fits (black). (E–H) Assumed changes in transmission due to pandemic perturbations (red) and estimated time-varying relative transmission rates for the perturbation impact from the SIRS model fits (black). Solid lines and shaded regions represent fitted posterior median and 95% credible intervals. (I–L) Comparisons between the true and estimated intrinsic resilience of the seasonally unforced system. Vertical lines represent the true intrinsic resilience of the seasonally unforced system. Density plots represent the posterior distribution of the inferred intrinsic resilience of the seasonally unforced SIRS model using fitted parameters.

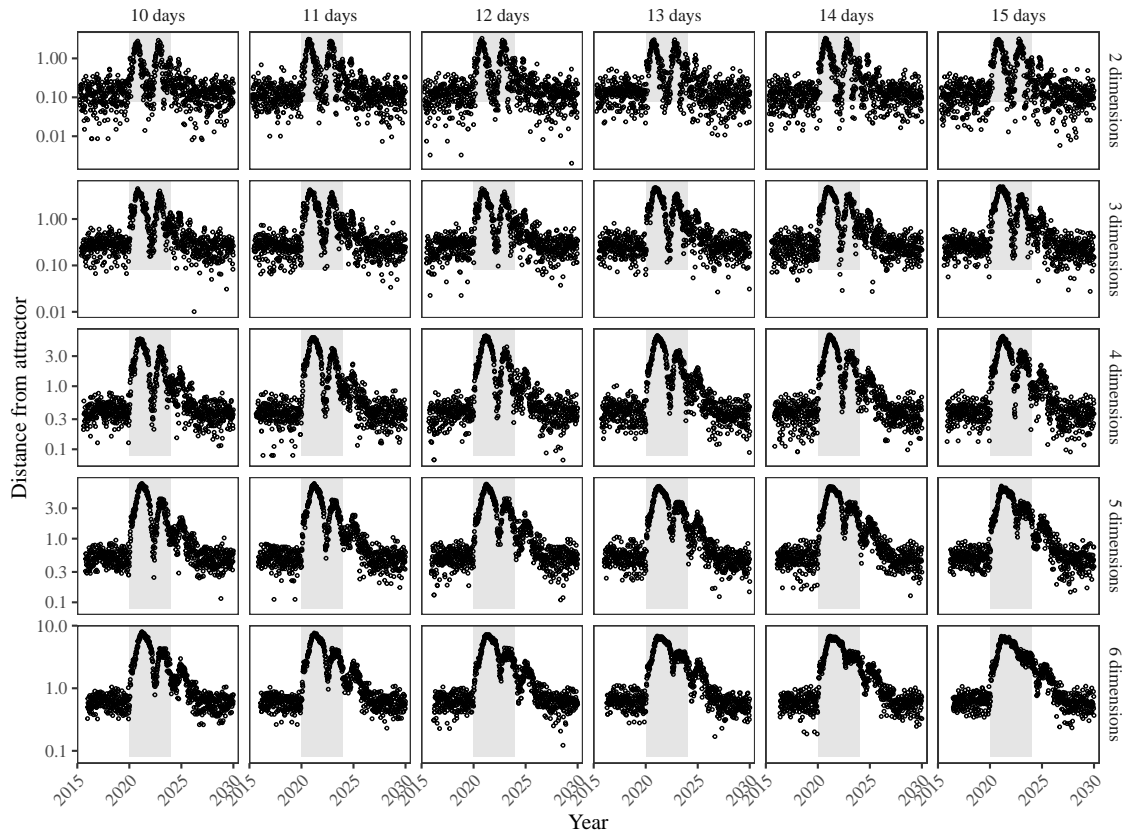


Figure S6: Sensitivity of the distance from the attractor to choice of embedding lags and dimensions. Sensitivity analysis for the distance-from-attractor time series shown in Figure 3E in the main text by varying the embedding lag between 10–15 days and embedding dimensions between 2–6 dimensions. The gray region represents the assumed period of pandemic perturbation.

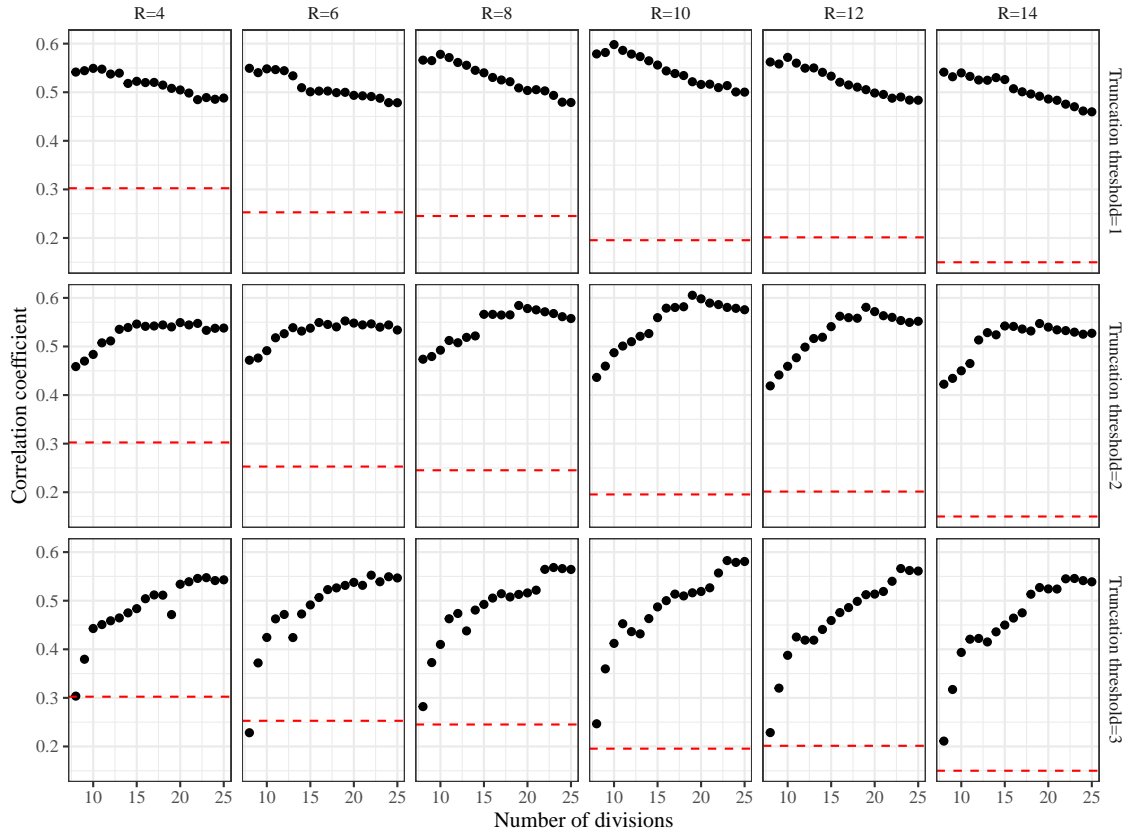


Figure S7: Impact of fitting window selection on the estimation of empirical resilience. We simulated 500 epidemics of a stochastic SIRS model with randomly drawn parameters and randomly generated pandemic perturbations (Supplementary Text). For each simulation, we varied the false nearest neighbor threshold R for reconstructing the empirical attractor as well as the parameters for regression window selection (i.e., the truncation threshold a and the number of divisions K). Each point represents the resulting correlation coefficient between empirical and intrinsic resilience estimates for a given scenario. Dashed lines represent the correlation coefficient between empirical and intrinsic resilience estimates for the naive approach that fits a linear regression on a log scale, starting from the maximum distance until the end of the time series.

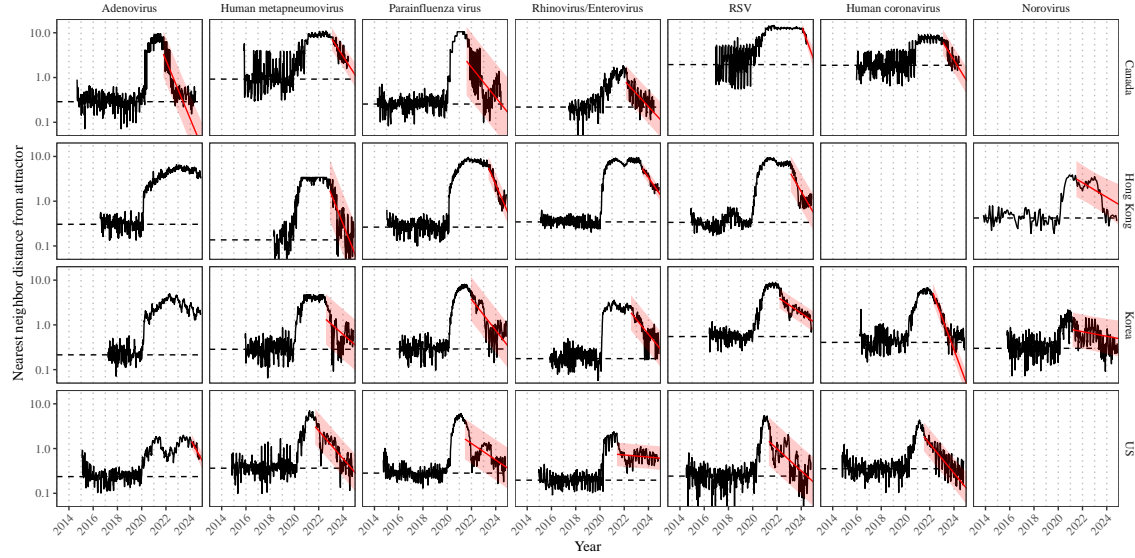


Figure S8: Estimated time series of distance from the attractor for each pathogen and corresponding linear regression fits using automated window selection criterion across Canada, Hong Kong, Korea, and the US. Black lines represent the estimated distance from the attractor. Red lines and shaded regions represent the linear regression fits and corresponding 95% confidence intervals. Dashed lines represent the average of the pre-pandemic nearest neighbor distances.

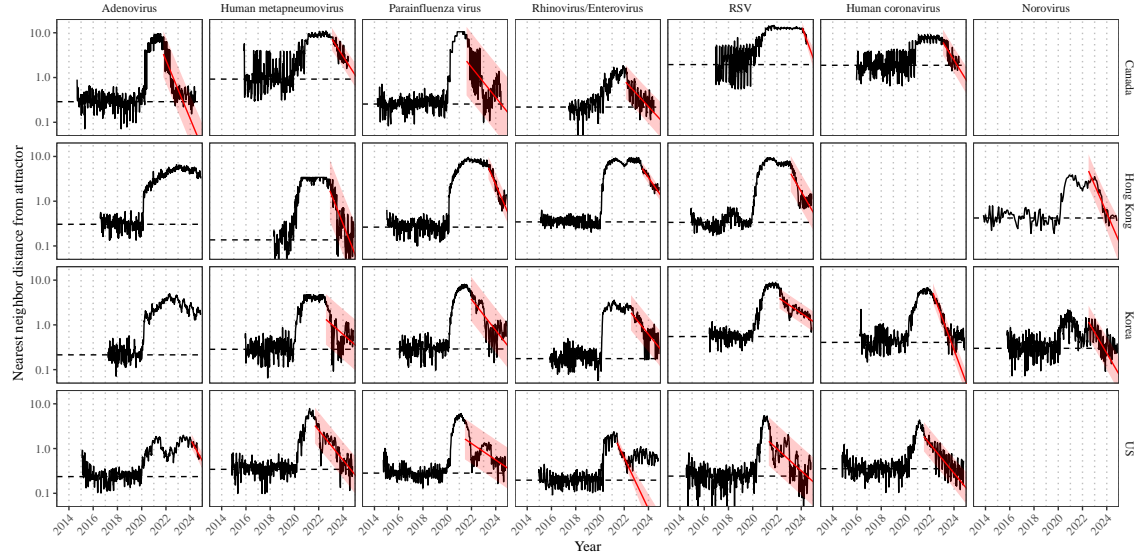


Figure S9: Estimated time series of distance from the attractor for each pathogen and corresponding linear regression fits across Canada, Hong Kong, Korea, and the US, including ad-hoc regression window selection. We used ad-hoc regression windows for norovirus in Hong Kong and Korea and rhinovirus/enterovirus in the US. Black lines represent the estimated distance from the attractor. Red lines and shaded regions represent the linear regression fits and corresponding 95% confidence intervals. Dashed lines represent the average of the pre-pandemic nearest neighbor distances.

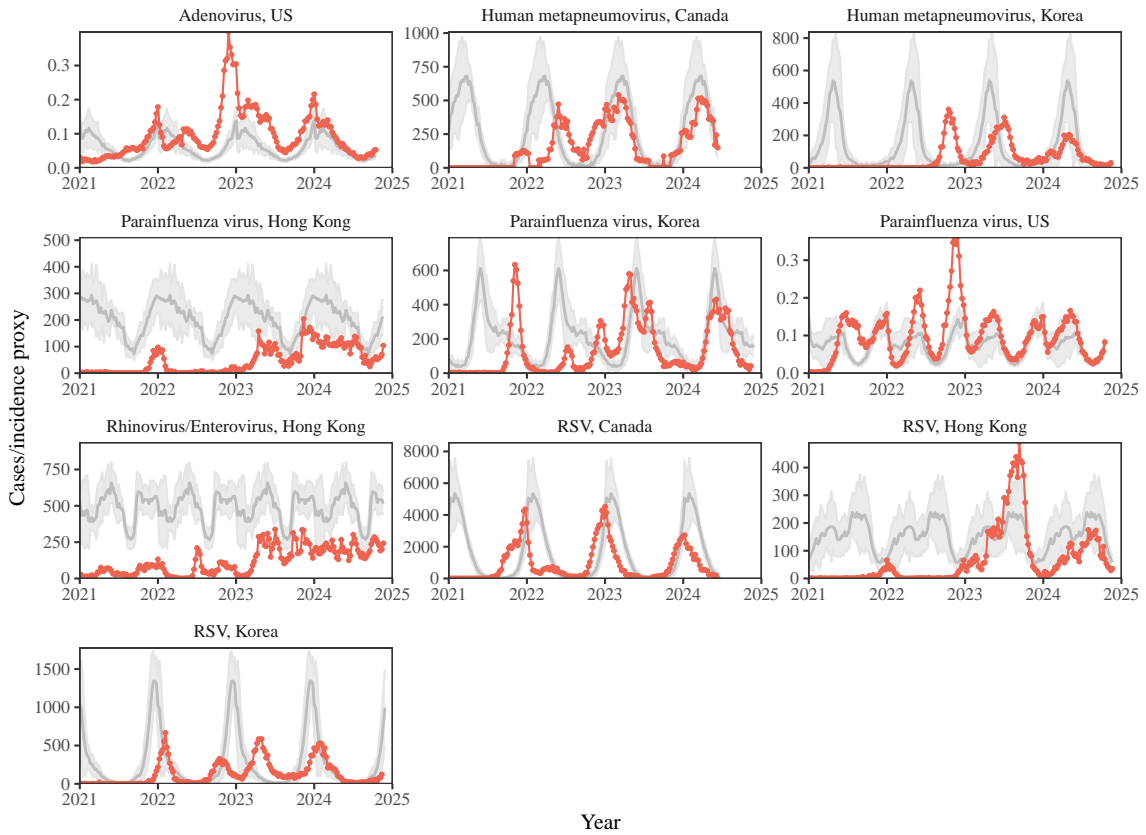


Figure S10: **Observed dynamics for pathogen that are predicted to return after the end of 2024.** Red points and lines represent data before 2020. Gray lines and shaded regions represent the mean seasonal patterns and corresponding 95% confidence intervals around the mean, previously shown in Figure 1.

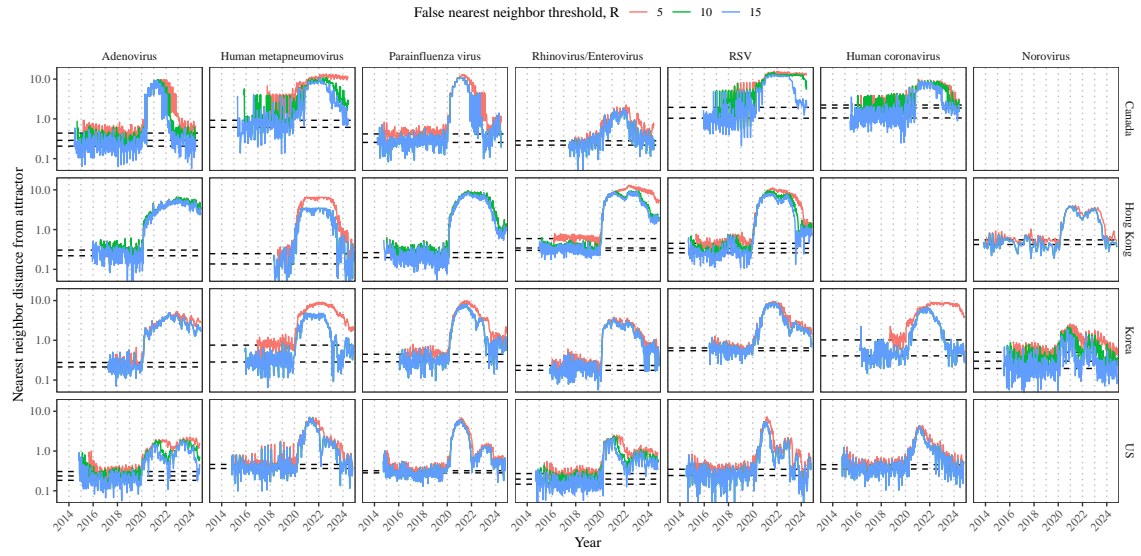


Figure S11: Estimated time series of distance from the attractor for each pathogen across different choices about false nearest neighbor threshold values. Using higher threshold values for the false nearest neighbor approach gives lower embedding dimensions. Colored lines represent the estimated distance from the attractor for different threshold values.

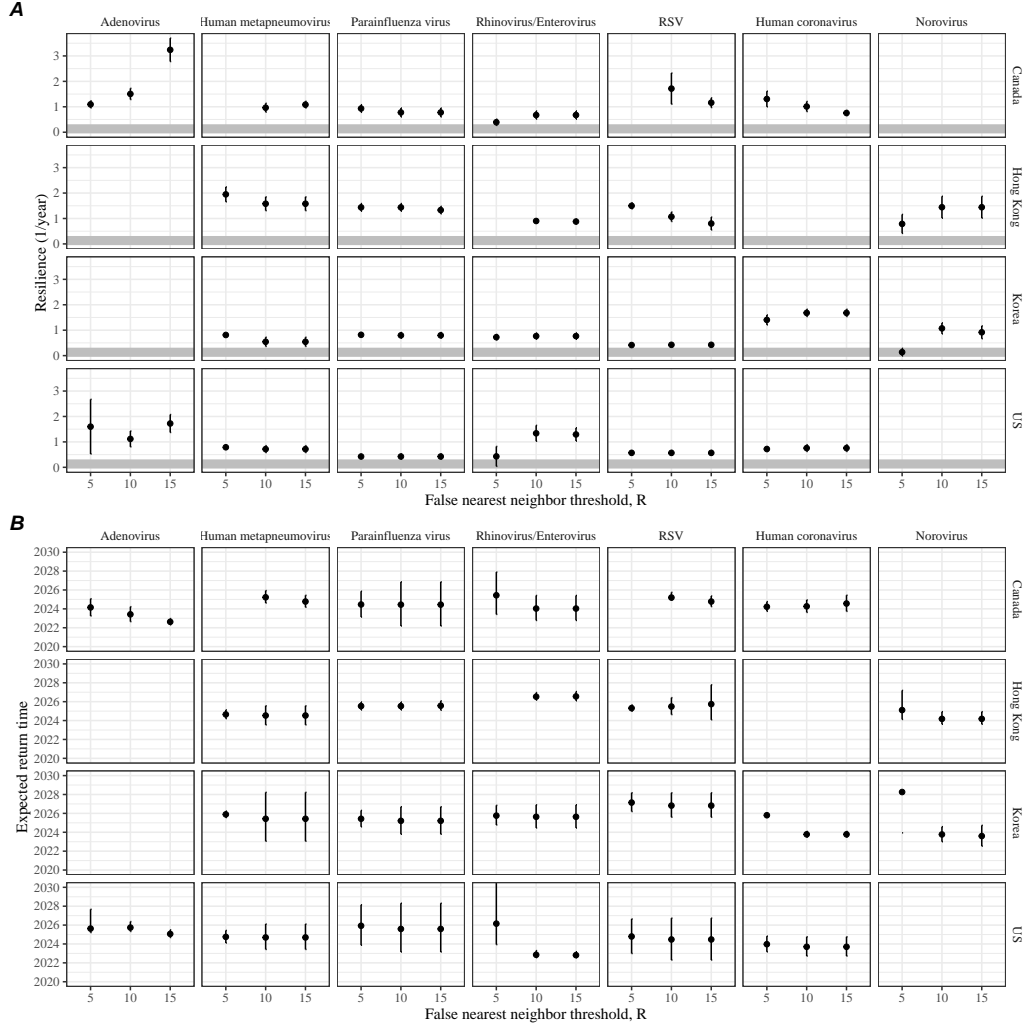


Figure S12: **Summary of resilience estimates and predictions for return time across different choices about false nearest neighbor threshold values.** The automated window selection method was used for all scenarios to estimate pathogen resilience, except for norovirus in Hong Kong and Korea and rhinovirus/enterovirus in the US. We used the same ad-hoc regression windows for norovirus in Hong Kong and Korea and rhinovirus/enterovirus in the US as we did in the main analysis. (A) Estimated pathogen resilience. The gray horizontal line represents the intrinsic resilience of pre-vaccination measles dynamics. (B) Predicted timing of when each pathogen will return to their pre-pandemic cycles. The dashed line in panel B indicates the end of 2024. Error bars represent 95% confidence intervals.

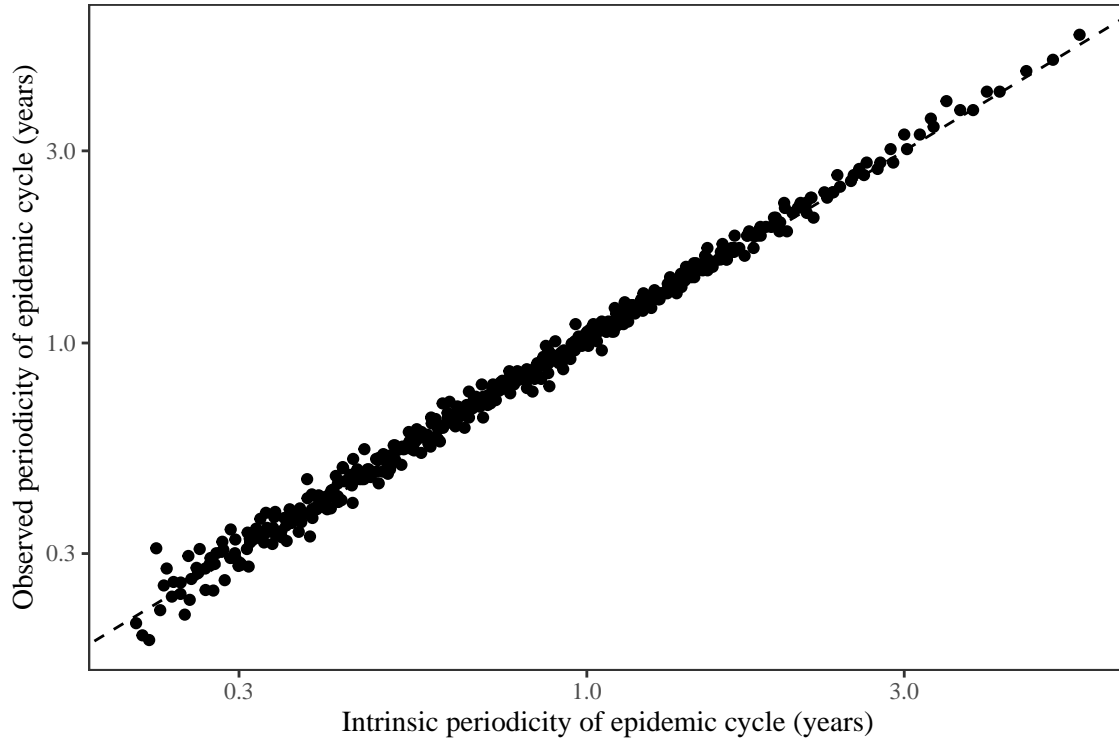


Figure S13: **Comparison between the observed and intrinsic periodicity of the epidemic cycle of the seasonally unforced SIRS model.** The observed periodicity of the epidemic corresponds to the periodicity at which maximum spectral density occurs. The intrinsic periodicity of the epidemic corresponds to $2\pi/\text{Im}(\lambda)$, where $\text{Im}(\lambda)$ is the imaginary part of the eigenvalue.

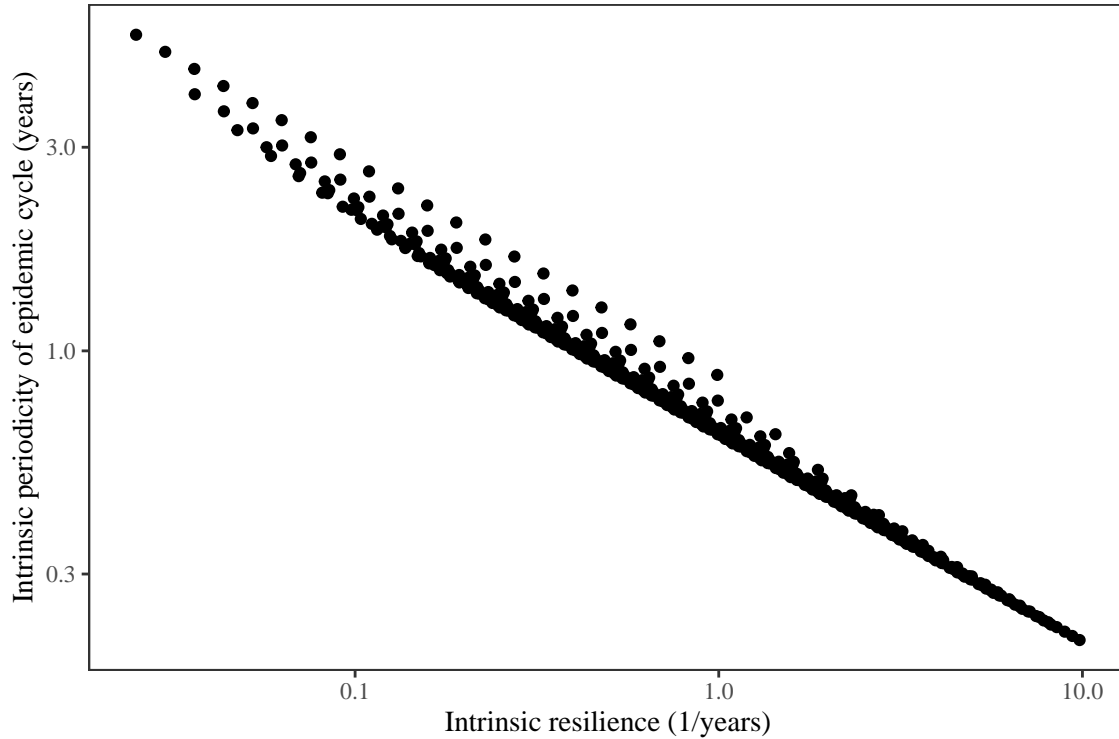


Figure S14: **Comparison between the intrinsic resilience and periodicity of the epidemic cycle of the seasonally unforced SIRS model.** The intrinsic resilience of the epidemic corresponds to the negative of the real value of the eigenvalue $-\text{Re}(\lambda)$. The intrinsic periodicity of the epidemic corresponds to $2\pi/\text{Im}(\lambda)$, where $\text{Im}(\lambda)$ is the imaginary part of the eigenvalue.

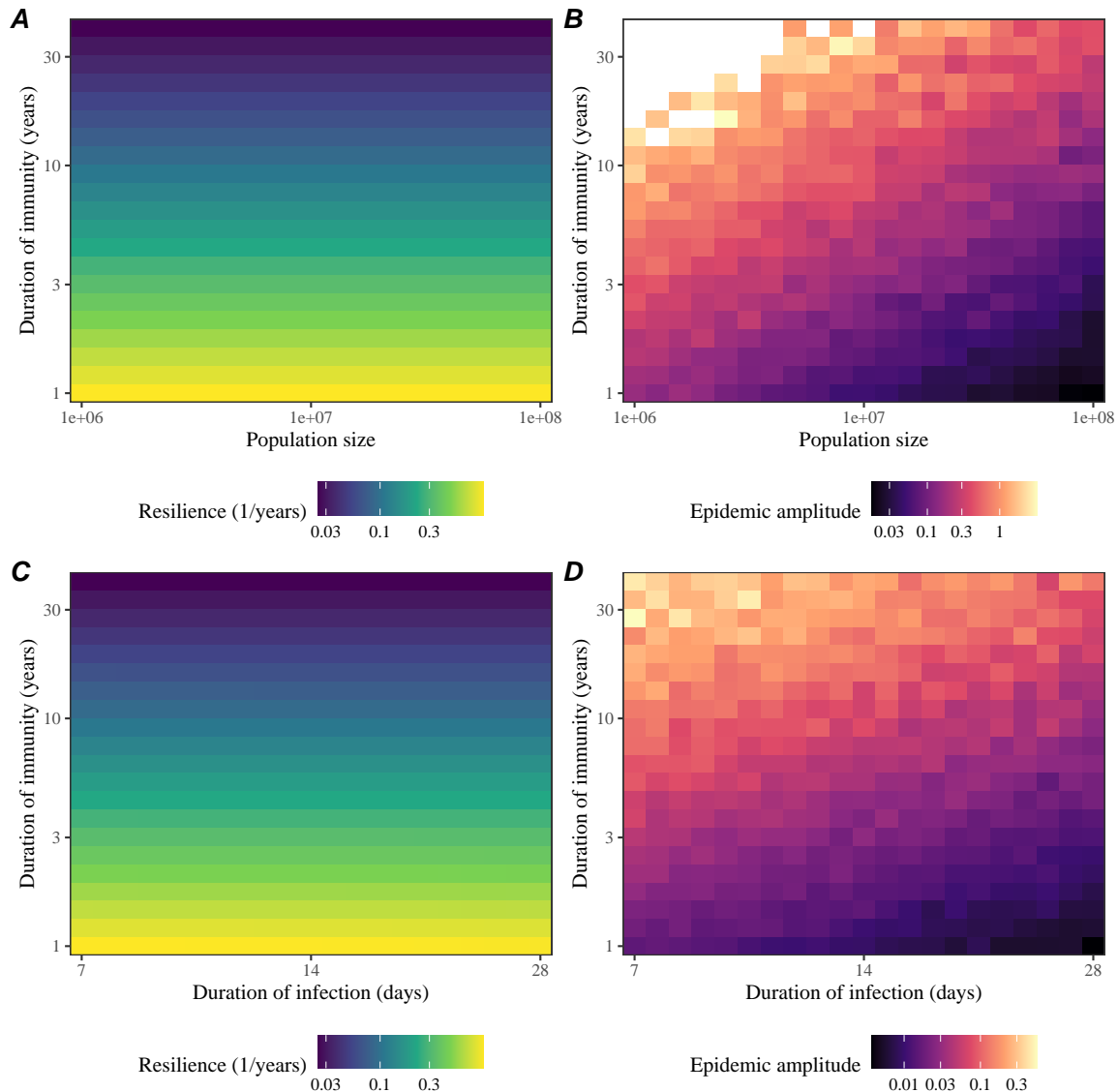


Figure S15: **Impact of population size and the average duration of infection of a host-pathogen system on its sensitivity to stochastic perturbations.** (A) Intrinsic resilience of a system as a function of population size and the average duration of immunity. (B) Epidemic amplitude as a function of population size and the average duration of immunity. (C) Intrinsic resilience of a system as a function of the average duration of infection and immunity. (D) Epidemic amplitude as a function of the average duration of infection and immunity. The epidemic amplitude corresponds to $(\max I - \min I)/(2\bar{I})$, where \bar{I} represents the mean prevalence.

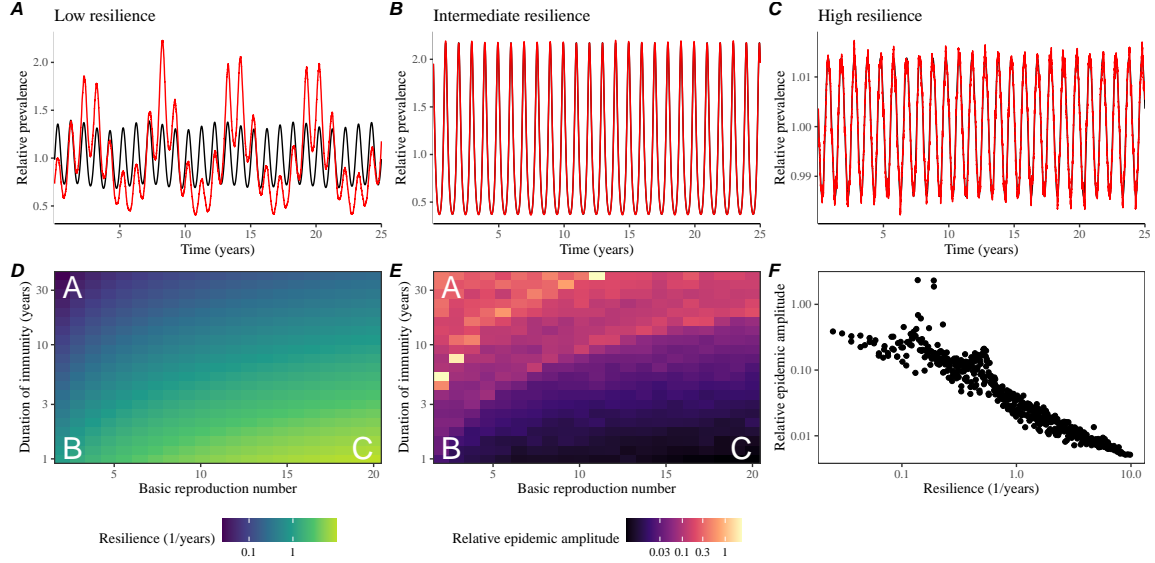


Figure S16: Linking resilience of a host-pathogen system to its sensitivity to stochastic perturbations for the seasonally forced SIRS model. (A–C) Epidemic trajectories of a stochastic SIRS model with demographic stochasticity across three different resilience values: low, intermediate, and high. The relative prevalence was calculated by dividing infection prevalence by its mean value. Black lines represent deterministic epidemic trajectories. Red lines represent stochastic epidemic trajectories. (D) The intrinsic resilience of the seasonally unforced system as a function of the basic reproduction number \mathcal{R}_0 and the duration of immunity. (E) The relative epidemic amplitude, a measure of sensitivity to stochastic perturbations, as a function of the basic reproduction number \mathcal{R}_0 and the duration of immunity. To calculate the relative epidemic amplitude, we first take the relative difference in infection prevalence between stochastic and deterministic trajectories: $\epsilon = (I_{\text{stoch}} - I_{\text{det}})/I_{\text{det}}$. Then, we calculate the difference between maximum and minimum of the relative difference and divide by half: $(\max \epsilon - \min \epsilon)/2$. Labels A–C in panels D and E correspond to scenarios shown in panels A–C. (F) The relationship between pathogen resilience and relative epidemic amplitude.

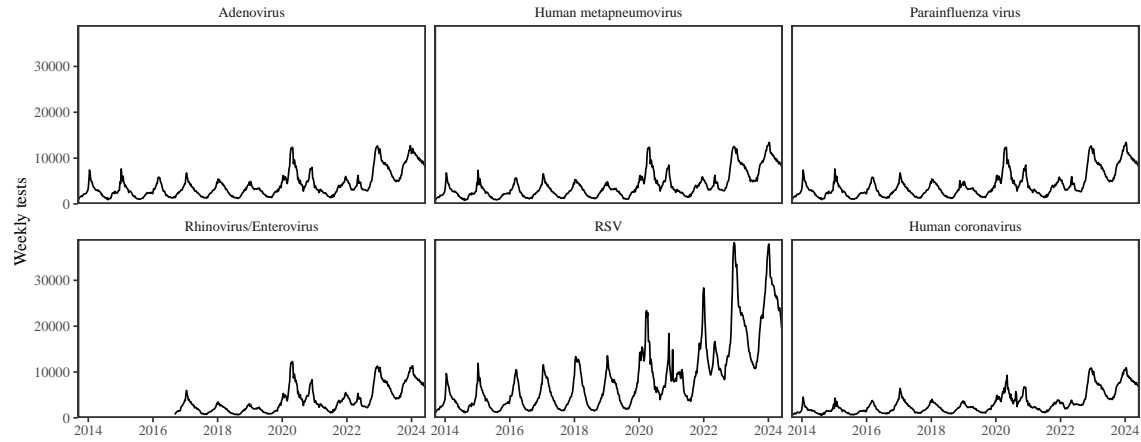


Figure S17: Testing patterns for respiratory pathogens in Canada.

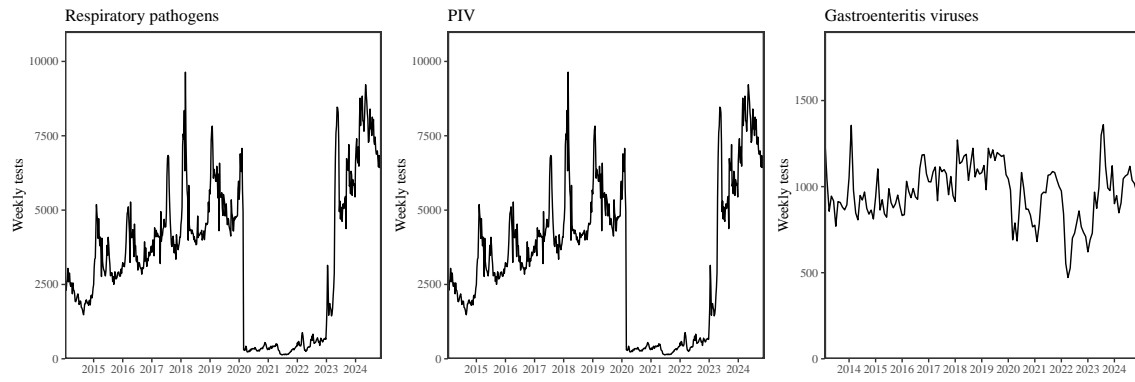


Figure S18: Testing patterns for respiratory pathogens, PIV, and gastroenteritis viruses in Hong Kong.

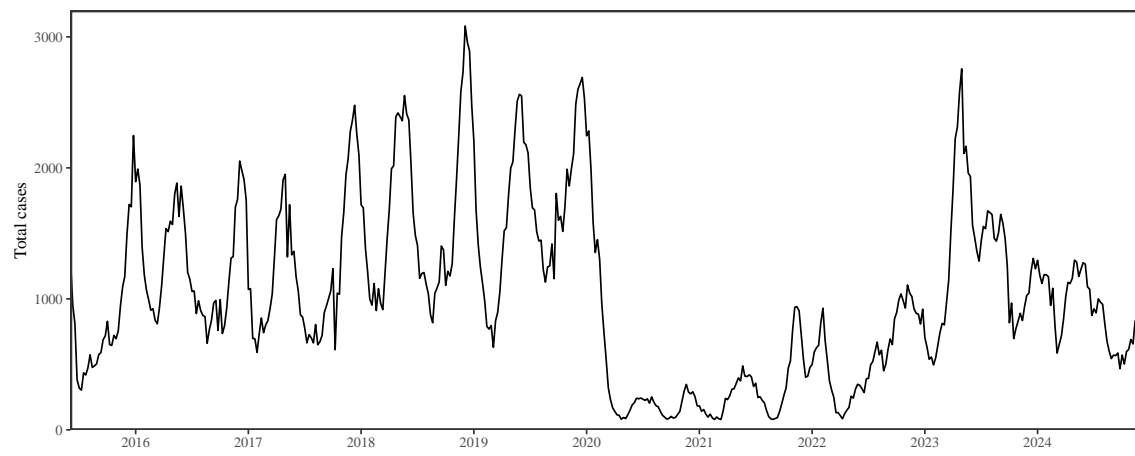


Figure S19: Total number of reported respiratory infection cases in Korea.

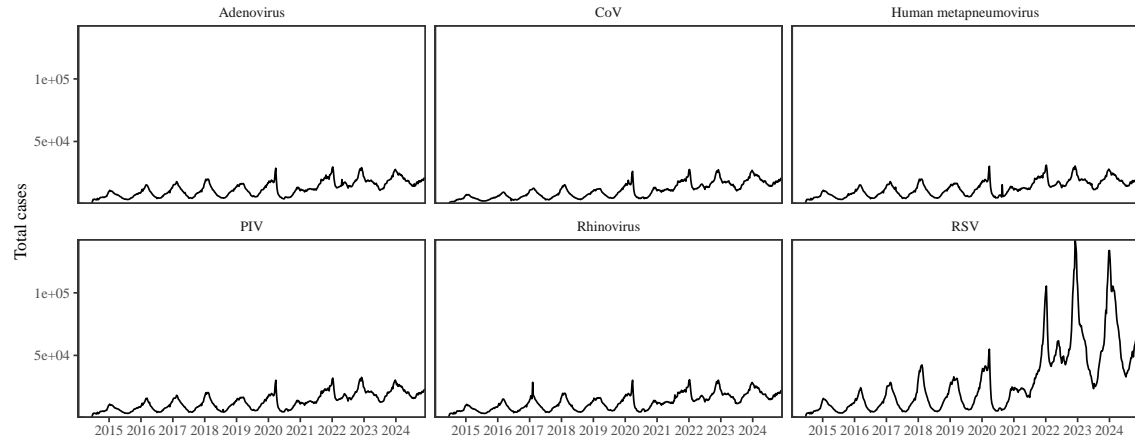


Figure S20: Testing patterns for respiratory pathogens in the US reported through the NREVSS.

806 **References**

- 807 [1] Rachel E Baker, Sang Woo Park, Wenchang Yang, Gabriel A Vecchi, C Jessica E
808 Metcalf, and Bryan T Grenfell. The impact of COVID-19 nonpharmaceutical
809 interventions on the future dynamics of endemic infections. *Proceedings of the*
810 *National Academy of Sciences*, 117(48):30547–30553, 2020.
- 811 [2] Gabriela B Gomez, Cedric Mahé, and Sandra S Chaves. Uncertain effects of the
812 pandemic on respiratory viruses. *Science*, 372(6546):1043–1044, 2021.
- 813 [3] Mihaly Koltai, Fabienne Krauer, David Hodgson, Edwin van Leeuwen, Marina
814 Treskova-Schwarzbach, Mark Jit, and Stefan Flasche. Determinants of RSV
815 epidemiology following suppression through pandemic contact restrictions. *Epi-*
816 *demics*, 40:100614, 2022.
- 817 [4] Sang Woo Park, Brooklyn Noble, Emily Howerton, Bjarke F Nielsen, Sarah
818 Lentz, Lilliam Ambroggio, Samuel Dominguez, Kevin Messacar, and Bryan T
819 Grenfell. Predicting the impact of non-pharmaceutical interventions against
820 COVID-19 on *Mycoplasma pneumoniae* in the United States. *Epidemics*,
821 49:100808, 2024.
- 822 [5] Amanda C Perofsky, Chelsea L Hansen, Roy Burstein, Shanda Boyle, Robin
823 Prentice, Cooper Marshall, David Reinhart, Ben Capodanno, Melissa Truong,
824 Kristen Schwabe-Fry, et al. Impacts of human mobility on the citywide trans-
825 mission dynamics of 18 respiratory viruses in pre-and post-COVID-19 pandemic
826 years. *Nature communications*, 15(1):4164, 2024.
- 827 [6] Eric J Chow, Timothy M Uyeki, and Helen Y Chu. The effects of the COVID-19
828 pandemic on community respiratory virus activity. *Nature Reviews Microbiol-*
829 *ogy*, 21(3):195–210, 2023.
- 830 [7] Stephen M Kissler, Christine Tedijanto, Edward Goldstein, Yonatan H Grad,
831 and Marc Lipsitch. Projecting the transmission dynamics of SARS-CoV-2
832 through the postpandemic period. *Science*, 368(6493):860–868, 2020.
- 833 [8] Rachel E Baker, Chadi M Saad-Roy, Sang Woo Park, Jeremy Farrar, C Jessica E
834 Metcalf, and Bryan T Grenfell. Long-term benefits of nonpharmaceutical inter-
835 ventions for endemic infections are shaped by respiratory pathogen dynamics.
836 *Proceedings of the National Academy of Sciences*, 119(49):e2208895119, 2022.
- 837 [9] Maaike C Swets, Clark D Russell, Ewen M Harrison, Annemarie B Docherty,
838 Nazir Lone, Michelle Girvan, Hayley E Hardwick, Leonardus G Visser, Pe-
839 ter JM Openshaw, Geert H Groeneveld, et al. SARS-CoV-2 co-infection with
840 influenza viruses, respiratory syncytial virus, or adenoviruses. *The Lancet*,
841 399(10334):1463–1464, 2022.

- 842 [10] Chun-Yang Lin, Joshua Wolf, David C Brice, Yilun Sun, Macauley Locke,
843 Sean Cherry, Ashley H Castellaw, Marie Wehenkel, Jeremy Chase Crawford,
844 Veronika I Zarnitsyna, et al. Pre-existing humoral immunity to human common
845 cold coronaviruses negatively impacts the protective SARS-CoV-2 antibody re-
846 sponse. *Cell host & microbe*, 30(1):83–96, 2022.
- 847 [11] Sam M Murray, Azim M Ansari, John Frater, Paul Klenerman, Susanna
848 Dunachie, Eleanor Barnes, and Ane Ogbe. The impact of pre-existing cross-
849 reactive immunity on SARS-CoV-2 infection and vaccine responses. *Nature*
850 *Reviews Immunology*, 23(5):304–316, 2023.
- 851 [12] John-Sebastian Eden, Chisha Sikazwe, Ruopeng Xie, Yi-Mo Deng, Sheena G
852 Sullivan, Alice Michie, Avram Levy, Elena Cutmore, Christopher C Blyth,
853 Philip N Britton, et al. Off-season RSV epidemics in Australia after easing
854 of COVID-19 restrictions. *Nature communications*, 13(1):2884, 2022.
- 855 [13] Stuart L Pimm. The structure of food webs. *Theoretical population biology*,
856 16(2):144–158, 1979.
- 857 [14] Michael G Neubert and Hal Caswell. Alternatives to resilience for measuring
858 the responses of ecological systems to perturbations. *Ecology*, 78(3):653–665,
859 1997.
- 860 [15] Lance H Gunderson. Ecological resilience—in theory and application. *Annual*
861 *review of ecology and systematics*, 31(1):425–439, 2000.
- 862 [16] Vasilis Dakos and Sonia Kéfi. Ecological resilience: what to measure and how.
863 *Environmental Research Letters*, 17(4):043003, 2022.
- 864 [17] Floris Takens. Detecting strange attractors in turbulence. In *Dynamical Sys-*
865 *tems and Turbulence, Warwick 1980: proceedings of a symposium held at the*
866 *University of Warwick 1979/80*, pages 366–381. Springer, 2006.
- 867 [18] Jonathan Dushoff, Joshua B Plotkin, Simon A Levin, and David JD Earn.
868 Dynamical resonance can account for seasonality of influenza epidemics. *Pro-*
869 , 101(48):16915–16916, 2004.
- 870 [19] Alan Hastings, Carole L Hom, Stephen Ellner, Peter Turchin, and H Charles J
871 Godfray. Chaos in ecology: is mother nature a strange attractor? *Annual review*
872 *of ecology and systematics*, pages 1–33, 1993.
- 873 [20] Alan Hastings, Karen C Abbott, Kim Cuddington, Tessa Francis, Gabriel Gell-
874 ner, Ying-Cheng Lai, Andrew Morozov, Sergei Petrovskii, Katherine Scran-
875 ton, and Mary Lou Zeeman. Transient phenomena in ecology. *Science*,
876 361(6406):eaat6412, 2018.

- 877 [21] P Rohani, CJ Green, NB Mantilla-Beniers, and Bryan T Grenfell. Ecological
878 interference between fatal diseases. *Nature*, 422(6934):885–888, 2003.
- 879 [22] Matthew B Kennel, Reggie Brown, and Henry DI Abarbanel. Determining
880 embedding dimension for phase-space reconstruction using a geometrical con-
881 struction. *Physical review A*, 45(6):3403, 1992.
- 882 [23] Eugene Tan, Shannon Algar, Débora Corrêa, Michael Small, Thomas Stemler,
883 and David Walker. Selecting embedding delays: An overview of embedding
884 techniques and a new method using persistent homology. *Chaos: An Interdis-*
885 *ciplinary Journal of Nonlinear Science*, 33(3), 2023.
- 886 [24] Bjarke Frost Nielsen, Sang Woo Park, Emily Howerton, Olivia Frost Lorentzen,
887 Mogens H Jensen, and Bryan T Grenfell. Complex multianual cycles of My-
888 coplasma pneumoniae: persistence and the role of stochasticity. *arXiv*, 2025.
- 889 [25] Samantha Bosis, Susanna Esposito, HGM Niesters, GV Zuccotti, G Marseglia,
890 Marcello Lanari, Giovanna Zuin, C Pelucchi, ADME Osterhaus, and Nicola
891 Principi. Role of respiratory pathogens in infants hospitalized for a first episode
892 of wheezing and their impact on recurrences. *Clinical microbiology and infection*,
893 14(7):677–684, 2008.
- 894 [26] Miguel L O’Ryan, Yalda Lucero, Valeria Prado, María Elena Santolaya, Marcela
895 Rabello, Yanahara Solis, Daniela Berrios, Miguel A O’Ryan-Soriano, Hector
896 Cortés, and Nora Mamani. Symptomatic and asymptomatic rotavirus and
897 norovirus infections during infancy in a Chilean birth cohort. *The Pediatric
898 infectious disease journal*, 28(10):879–884, 2009.
- 899 [27] Virginia E Pitzer, Cécile Viboud, Wladimir J Alonso, Tanya Wilcox, C Jessica
900 Metcalf, Claudia A Steiner, Amber K Haynes, and Bryan T Grenfell. Environ-
901 mental drivers of the spatiotemporal dynamics of respiratory syncytial virus in
902 the United States. *PLoS pathogens*, 11(1):e1004591, 2015.
- 903 [28] Arthur WD Edridge, Joanna Kaczorowska, Alexis CR Hoste, Margreet Bakker,
904 Michelle Klein, Katherine Loens, Maarten F Jebbink, Amy Matser, Cormac M
905 Kinsella, Paloma Rueda, et al. Seasonal coronavirus protective immunity is
906 short-lasting. *Nature medicine*, 26(11):1691–1693, 2020.
- 907 [29] Jennifer M Radin, Anthony W Hawksworth, Peter E Kammerer, Melinda Bal-
908 ansay, Rema Raman, Suzanne P Lindsay, and Gary T Brice. Epidemiology
909 of pathogen-specific respiratory infections among three US populations. *PLoS
910 One*, 9(12):e114871, 2014.
- 911 [30] Guojian Lv, Limei Shi, Yi Liu, Xuecheng Sun, and Kai Mu. Epidemiological
912 characteristics of common respiratory pathogens in children. *Scientific Reports*,
913 14(1):16299, 2024.

- 914 [31] Saverio Caini, Adam Meijer, Marta C Nunes, Laetitia Henaff, Malaika Zounon,
915 Bronke Boudewijns, Marco Del Riccio, and John Paget. Probable extinction of
916 influenza b/yamagata and its public health implications: a systematic literature
917 review and assessment of global surveillance databases. *The Lancet Microbe*,
918 2024.
- 919 [32] Zhiyuan Chen, Joseph L-H Tsui, Bernardo Gutierrez, Simon Busch Moreno,
920 Louis du Plessis, Xiaowei Deng, Jun Cai, Sumali Bajaj, Marc A Suchard,
921 Oliver G Pybus, et al. COVID-19 pandemic interventions reshaped the global
922 dispersal of seasonal influenza viruses. *Science*, 386(6722):eadq3003, 2024.
- 923 [33] Hai Nguyen-Tran, Sang Woo Park, Kevin Messacar, Samuel R Dominguez,
924 Matthew R Vogt, Sallie Permar, Perdita Permaul, Michelle Hernandez, Daniel C
925 Douek, Adrian B McDermott, et al. Enterovirus D68: a test case for the use of
926 immunological surveillance to develop tools to mitigate the pandemic potential
927 of emerging pathogens. *The Lancet Microbe*, 3(2):e83–e85, 2022.
- 928 [34] Bryan T Grenfell, Ottar N Bjørnstad, and Bärbel F Finkenstädt. Dynamics of
929 measles epidemics: scaling noise, determinism, and predictability with the TSIR
930 model. *Ecological monographs*, 72(2):185–202, 2002.
- 931 [35] Samit Bhattacharyya, Per H Gesteland, Kent Korgenski, Ottar N Bjørnstad,
932 and Frederick R Adler. Cross-immunity between strains explains the dynamical
933 pattern of paramyxoviruses. *Proceedings of the National Academy of Sciences*,
934 112(43):13396–13400, 2015.
- 935 [36] Katharine R Dean, Fabienne Krauer, Lars Walløe, Ole Christian Lingjærde, Bar-
936 Barbara Bramanti, Nils Chr Stenseth, and Boris V Schmid. Human ectoparasites
937 and the spread of plague in Europe during the Second Pandemic. *Proceedings
938 of the National Academy of Sciences*, 115(6):1304–1309, 2018.
- 939 [37] Margarita Pons-Salort and Nicholas C Grassly. Serotype-specific immunity
940 explains the incidence of diseases caused by human enteroviruses. *Science*,
941 361(6404):800–803, 2018.
- 942 [38] Sarah Cobey and Edward B Baskerville. Limits to causal inference with state-
943 space reconstruction for infectious disease. *PloS one*, 11(12):e0169050, 2016.
- 944 [39] Public Health Agency of Canada. Respiratory virus detections in
945 Canada. 2024. <https://www.canada.ca/en/public-health/services/surveillance/respiratory-virus-detections-canada.html>. Accessed Sep
946 4, 2024.
- 948 [40] Centre for Health Protection. Detection of pathogens from respiratory spec-
949 imens. 2024. <https://www.chp.gov.hk/en/statistics/data/10/641/642/2274.html>. Accessed Nov 20, 2024.

- 951 [41] Centre for Health Protection. Detection of gastroenteritis viruses from faecal
952 specimens. 2024. <https://www.chp.gov.hk/en/statistics/data/10/641/717/3957.html>. Accessed Nov 20, 2024.
- 954 [42] Korea Disease Control and Prevention Agency. Acute respiratory infection,
955 Sentinel surveillance infectious diseases. 2024. <https://dportal.kdca.go.kr/pot/is/st/ari.do>. Accessed Nov 20, 2024.
- 957 [43] Edward Goldstein, Sarah Cobey, Saki Takahashi, Joel C Miller, and Marc Lipsitch. Predicting the epidemic sizes of influenza A/H1N1, A/H3N2, and B: a
958 statistical method. *PLoS medicine*, 8(7):e1001051, 2011.
- 960 [44] Karline Soetaert, Thomas Petzoldt, and R Woodrow Setzer. Solving differential
961 equations in R: package deSolve. *Journal of statistical software*, 33:1–25, 2010.
- 962 [45] R Core Team. *R: A Language and Environment for Statistical Computing*. R
963 Foundation for Statistical Computing, Vienna, Austria, 2023.
- 964 [46] Sang Woo Park, Inga Holmdahl, Emily Howerton, Wenchang Yang, Rachel E
965 Baker, Gabriel A Vecchi, Sarah Cobey, C Jessica E Metcalf, and Bryan T Grenfell. Interplay between climate, childhood mixing, and population-level suscep-
966 tibility explains a sudden shift in RSV seasonality in Japan. *medRxiv*, pages
967 2025–03, 2025.
- 969 [47] Bob Carpenter, Andrew Gelman, Matthew D Hoffman, Daniel Lee, Ben
970 Goodrich, Michael Betancourt, Marcus A Brubaker, Jiqiang Guo, Peter Li,
971 and Allen Riddell. Stan: A probabilistic programming language. *Journal of
972 statistical software*, 76, 2017.
- 973 [48] Stan Development Team. RStan: the R interface to Stan, 2024. R package
974 version 2.32.6.